Accelerated erosion and sediment fluxes in the Ayeyarwady River due to anthropogenic activities

Xiaolong Dong[1], Xiumian Hu[1*], Guangwei Li[1*], Eduardo Garzanti[2], Yani Najman[3], Wendong Liang[4], Yuntao Tian[5], Jiangang Wang[6]

(1) State Key Laboratory of Critical Earth Material Cycling and Mineral Deposits, School of Earth Sciences and Engineering, Nanjing University, Nanjing 210023, China

(2) Laboratory for Provenance Studies, Department of Earth and Environmental Sciences, University of Milano-Bicocca, Milano 20126, Italy

(3) Lancaster Environment Centre, Lancaster University, Lancaster LA1 4YQ, UK

(4) State Key Laboratory of Oil and Gas Reservoir Geology and Exploitation, Institute of Sedimentary Geology, Chengdu University of Technology, Chengdu 610059, China

(5) Guangdong Provincial Key Lab of Geodynamics and Geohazards, School of Earth Sciences and Engineering, Sun Yat-sen University, Guangzhou 510275, China

(6) State Key Laboratory of Lithospheric and Environmental Coevolution, Institute of Geology and Geophysics, Chinese Academy of Sciences, Beijing 100029, China

*Corresponding authors: Xiumian Hu (huxm@nju.edu.cn); Guangwei Li (guangweili@nju.edu.cn)

Abstract

Human activities have a strong impact on global climate and natural ecosystems, yet the extent of their influence on long-term natural erosional processes remains poorly determined. A quantitative analysis is needed. The Ayeyarwady River, renowned for its large sediment flux ranking second in Asia, provides a compelling case study. We here show that extensive alluvial mining in the Ayeyarwady catchment has strongly accelerated erosion rates compared to natural benchmark levels, thereby contributing to its high sediment discharge. To highlight this point, we assessed present-day erosion rates in diverse catchments by comparing gauged sediment fluxes with long-term natural erosion rates derived from detrital-apatite fission track (AFT) and cosmogenic ^{10}Be data. Our findings reveal a stark contrast. Long-term natural erosion rates were notably higher in the Upper Ayeyarwady (0.06-0.34 mm/a) than in the Upper Chindwin (0.02 ± 0.005 mm/a), whereas present-day erosion rates are three times higher in the Upper Chindwin (0.63 ± 0.05 mm/a) than in the Upper Ayeyarwady (0.19 ± 0.02 mm/a). Particularly noteworthy are the Upper Chindwin and Mu drainages, where erosion rates are calculated to have increased by more than an-order-of-magnitude relative to long-term natural background rates. Such a striking increase in erosion rate correlates positively with the spatial distribution of alluvial mining, suggesting that anthropogenic activities represent an important contributor to the sediment discharge of the modern Ayeyarwady River, especially for the Upper Chindwin catchment. The observed increases in sediment fluxes from long-term to present-day timescales across the Chindwin, Upper Ayeyarwady, and entire Ayeyarwady catchments may also be attributed to by land-use expansion related deforestation, and intensified precipitation in the 20th-century. These results underscore how human activities can drastically accelerate erosional processes, thus exerting a dramatic impact on natural systems.

Plain Language Summary

Human activities are known to significantly affect global climate and natural ecosystems, but their impact on long-term erosional processes remains to be quantitatively assessed. In this study, we show that extensive alluvial mining in the Ayeyarwady catchment has strongly accelerated erosion compared to natural background levels, thereby contributing to its very high sediment discharge. By comparing modern erosion rates with long-term natural erosion rates, we discovered a major discrepancy. Natural erosion rates were much higher in the Upper Ayeyarwady basin than in the Upper Chindwin basin. But, in stark contrast, present-day erosion rates are three times higher in the Upper Chindwin than in the Upper Ayeyarwady. The erosion rates in the Upper Chindwin and Mu drainage basins are calculated to have increased by more than one order of magnitude relative to past natural erosion rates.

These findings reveal a strong link between mining and increased sediment discharge, with land-use expansion related deforestation, and increasing precipitation in the 20th-century making contributions to all Ayeyarwady sub-catchments. This study shows that human activities can dramatically accelerate erosion, strongly impacting sediment discharge, natural landscapes, and ecosystems.

Key Points

- Long-term natural erosion rates were higher in the Upper Ayeyarwady than in the Upper Chindwin (0.06-0.34 mm/a *vs.* 0.02 mm/a)
- Present-day erosion rates are higher in the Upper Chindwin (0.63 ± 0.05 mm/a), where they increased by more than one order of magnitude
- Anthropogenic activities represent an important contributor to sediment discharge of the modern Ayeyarwady River

Key words: Anthropocene, Human impact, Long-term erosion rates, Present-day erosion rates, Ayeyarwady

1. Introduction

Human activities can significantly influence erosion at decadal to annual timescales thus accelerating sediment production in river catchments by deforestation (e.g., in the southern Ecuadorian Andes; Vanacker et al., 2007), agricultural land use (e.g., Sri Lanka; Hewawasam et al., 2003), and alluvial mining (e.g., global tropical rivers; Dethier et al., 2023). Recent remote-sensing research has shown that alluvial mining has notably increased sediment load in tropical drainages since 1990 (Dethier et al., 2023). Human impact on sediment production began 3000 years ago and markedly accelerated in the last thousand years (Best, 2018; Syvitski and Kettner, 2011). Remote-sensing techniques, however, were able to detect such changes only since the 1980s and quantifying the extent of accelerated erosion and sediment discharge relative to natural background fluxes remains a challenge despite such recognized impacts (Best, 2018; Lindert, 2000).

The Ayeyarwady (Irrawaddy) River, draining most of Myanmar, ranks second in Asia in terms of sediment fluxes (Figure 1a); flux is particularly high in the Upper Chindwin catchment, a major tributary of the Ayeyarwady (Figure 1b). Previous studies estimated that the Chindwin River contributes more than half of the Ayeyarwady sediment load despite covering only ~26% of the total catchment area (Garzanti et al., 2016). Such a high sediment contribution was primarily ascribed to the higher erodibility of siliciclastic rocks widely exposed in the Chindwin catchment (Garzanti et al., 2016). However, the potential impact of anthropogenic activities such as extensive jade and gold mining (Shrestha et al., 2020) was not considered. To investigate the potential anthropogenic impact, a combined approach is here applied to quantify the human-induced increment of sediment production relative to natural background values by comparing present-day to long-term natural erosion rates. Present-day erosion rates were calculated directly from gauged suspended-load and reported modeled bedload data wherever available (Cohen et al., 2022), combined with forward mixing modeling (Garzanti et al., 2012) in sub-catchments where gauged data are unavailable. Long-term natural erosion rates were inferred from both numerical inversion of detrital AFT ages (million-year timescale) and cosmogenic ^{10}Be (thousand-year timescale). The comparison of these independent datasets highlights how the very high present-day sediment fluxes in the Ayeyarwady River largely result from anthropic activities. This study thus underscores the impact that human activities may have on the acceleration of erosion and on sediment fluxes in large river systems.

2. The Ayeyarwady River

The Ayeyarwady River (drainage basin ~430,000 km^2) flows southward across Myanmar for ~2170 km and forms a large delta distributary network before discharging into the Andaman Sea. The Upper Ayeyarwady originates from the confluence of the Nmai and Mali headwater branches, both sourced from high mountain glaciers in northernmost Myanmar, ~280 km southeast of the eastern Himalaya syntaxis (Figures

1a and 1b). The Upper Ayeyarwady upstream of the Chindwin confluence is joined from north to south by the Taping, Shweli and Myitnge left-bank tributaries, and farther downstream by the Mu River near Sagaing. The principal tributary by far is the Chindwin River, which runs southward along the eastern edge of the Indo-Myanmar Ranges, receives its left-bank Uyu and right-bank Myitha tributaries, and finally joins the Ayeyarwady River to the southeast of Mandalay. Only minor tributaries contribute to the Lower Ayeyarwady between the Chindwin confluence and the sea.

2.1. Hydrology and sediment flux

Most of the Ayeyarwady basin is dominated by the southwest Asian monsoon and thus characterized by tropical monsoonal climate, with most precipitation and discharge between June and September (Zaw et al., 2017). Rainfall varies markedly across the basin, from ~500 mm in central areas to 4,000 mm in northern mountainous regions (Sirisena et al., 2021) (Figure 1c). Average and maximum water discharge are estimated to be 12,000 m^3/s and 42,100 m^3/s, respectively (Baronas et al., 2020).

The Ayeyarwady River is less regulated compared to other major rivers in Asia, such as the Yangtze, Mekong, or Salween (Wang et al., 2011; Dethier et al., 2022). There are no large dams on the main river and only small dams exist on a few tributaries (Schmitt et al., 2021). The annual suspended-load flux of the Ayeyarwady River at Pyay was estimated as 326^{+91}_{-70} million tons (Mt) in 2017-2019 (Baronas et al., 2020), consistent with previous estimates of 325 ± 57 Mt (Furuichi et al., 2009) and 364 ± 60 Mt (Robinson et al., 2007). Notably lower figures (265 Mt) were estimated in the nineteenth-century (Gordon, 1885). The two main branches, the Chindwin and the Upper Ayeyarwady, contributed annually ~120 Mt at Kalewa over the period 1991-2010 (Sirisena et al., 2021) and ~64 Mt at Sagaing (International Finance Corporation (IFC), 2017), between 1990 and 2010.

2.2. Geological background

The Ayeyarwady catchment can be subdivided into four main geological domains

(Figure 1b): the Indo-Myanmar Ranges (IMR) in the west, the Central Myanmar Basin (CMB), the Mogok Metamorphic Belt (MMB) in the north, and the Shan Plateau in the east. The IMR, located to the west of the Kabaw Fault, is a Mesozoic-Cenozoic accretionary prism (Betka et al., 2018), comprising Triassic schists, Jurassic ophiolites, and Cretaceous sedimentary rocks in the IMR core (Brunnschweiler, 1966; Suzuki et al., 2004), Eocene sedimentary rocks in the Inner IMR (Mitchell, 1993; Naing et al., 2014), and Neogene strata in the Outer IMR (Allen et al., 2008). The CMB hosts a ≥ 10-km-thick Cretaceous to Quaternary forearc and backarc basin succession accumulated in various depocenters separated by the mid-Cretaceous-Miocene Wuntho-Popa Arc (Kyaw Linn et al., 2015; Licht et al., 2020). The MMB is an elongated domain of up to high-grade metamorphic rocks and Permian to Miocene granitic intrusions, separated by the ophiolite-bearing belt from Precambrian metamorphic basement and Triassic turbidites of the Katha Gangaw Range in the west (e.g., Mitchell et al., 2012) (Figure 1b). The easternmost domain, the Shan Plateau, exposes Neoproterozoic-Paleozoic sedimentary rocks intruded by Cambrian to Mesozoic granitoids (Bender, 1983).

3. Sampling and methods

In 2013 and 2020, fifteen fine to medium sand samples were collected from active fluvial bars along the Ayeyarwady River and its major tributaries from northern Myanmar headwaters to the Ayeyarwady Delta. Sampling sites were selected away from the tributaries conference and urban or village areas to make samples representative. Prior to collection, the top 10 cm of surface sand was removed to minimize wind disturbance effects. Ten new sand samples were analyzed for framework petrography and heavy minerals, while five headwater samples, previously analyzed by Garzanti et al. (2016), were also included. Additionally, thirteen samples were selected for detrital apatite fission track (AFT) analysis, and nine were used for cosmogenic ^{10}Be measurement. Full information on sample locations is provided in Supporting

Information S2, Tables S1.

3.1. Petrography and heavy minerals analysis

Ten sand samples (seven from the mainstem and one each from the Chindwin, Mu, and Yaw rivers) were analyzed for petrography and heavy minerals to calculate a provenance budget (Supporting Information S2, Tables S2, S3). From each sand sample, a quartered fraction of the 63-2000 μm class obtained by wet sieving was impregnated with araldite epoxy and cut into a standard thin section. Petrographic analyses were carried out by counting more than 400 points on each thin section according to the Gazzi-Dickinson method (Ingersoll et al., 1984). Sand classification was based on the relative abundance of the three main framework components quartz (Q), feldspars (F), and lithic fragments (L), considered if exceeding 10% QFL (Garzanti, 2019).

From a split aliquot of the 32-500 μm size window obtained by wet sieving, heavy minerals were separated by centrifuging in Na-polytungstate (2.90 g/cm^3). More than 200 transparent heavy minerals (tHM) were point-counted at appropriate regular spacing to minimize overestimation of smaller grains (Garzanti and Andò, 2019). Dubious grains were checked by Raman spectroscopy (Andò and Garzanti, 2014). The source rock density (SRD; g/cm^3) index is the weighted average density of terrigenous grains calculated from point-counting mineralogical data. According to the transparent-heavy-mineral concentration (tHMC) in the sample, tHM suites are defined as very poor (tHMC $<$ 0.5), poor (0.5 $\leqslant$ tHMC $<$ 1), moderately poor (1 $\leqslant$ tHMC $<$ 2), moderately rich (2 $\leqslant$ tHMC $<$ 5), rich (5 $\leqslant$ tHMC $<$ 10) or very rich (tHMC $\geqslant$ 10) (Garzanti and Andò, 2007). The complete dataset is provided in Supporting Information S2, Tables S2, S3.

3.2. Apatite fission track (AFT) analysis and calculation of erosion rates at million-year timescale

Detrital AFT analyses were performed on thirteen sand samples using the LA-ICP-MS method (Hasebe et al., 2004). Polished mounts embedded with apatite grains were etched in 5 *M* HNO_3 at 20°C for 20 s to reveal spontaneous fission tracks (Barbarand et al., 2003). Fission-track counting was carried out using a Zeiss Axio Imager M2m microscope. Stacks of high-resolution digital images of each selected grain were then captured by TrackWorks with a ×100 dry objective under both transmitted and reflected light using a highly-sensitive and fast iDS camera at Nanjing University. Track counting was performed manually in *FastTracks* using the coincidence mapping technique (Gleadow et al., 2009). The etch pit diameter (*Dpar*) of selected grains was also determined. Uranium concentration in each counted grain was determined by LA-ICP-MS using an Agilent 8900 ICP–QQQ with an ESI New Wave NWR 193UC (TwoVol2) laser ablation system at the Beijing Quick-Thermo Science & Technology Co., Ltd. NIST SRM 612 glass was used to calibrate trace elements using calcium as internal standard. Reference materials were analyzed twice, before and after each analytical session, each time including 8 spots. Ablation on selected grains and reference materials was carried out for 30 s after ~10 s baseline signal collection, using a 30 µm or 40 µm diameter beam size according to apatite grain size, operated at ~3 J/cm^2 fluence with 5 Hz repetition rate. Because of large uncertainties, apatite grains with uranium concentration < 2 ppm were excluded from further analysis. In this study, 1,270 single-grain AFT ages were obtained from 13 samples (Figure 3); 35 grains were excluded from age calculations because of their low uranium concentration (< 2 ppm) and consequently high age uncertainties. The complete datasets are provided in Supporting Information S2, Tables S4.

3.3. Calculation of catchment-wide erosion rates at million-year timescales from detrital cooling ages

Million-year timescale exhumation rates were obtained from inversion modeling of detrital AFT ages based on age-elevation relationship. Fission-induced damage tracks in apatite are annealed at temperatures over 60-120°C (Gallagher, 1998), so that fission-track ages reflect cooling associated with exhumation from crustal depths of 2–5 km. We employed a Bayesian estimation of erosion model implemented with

MATLAB (Avdeev et al., 2011), which has been shown to efficiently invert temporally variable erosion histories from detrital dates. The applied approach relies on the primary assumption that sands were derived from a catchment with a monotonic positive thermochronological age-elevation (or depth) relationship. Based on this assumption and using a detritus sampling function, a distribution of detrital dates can be predicted. To compare predictions against observations, the goodness of the assumed age-elevation (or depth) relationship was evaluated and optimized through computational iterations. Finally, a catchment erosional history was derived from the slopes of the optimal age-elevation (or depth) relationship, as illustrated in previous studies (Ye et al., 2022; Zhuang et al., 2018).

We assumed a vertical exhumation pathway and a flat closure isotherm, so that, bedrock ages are a function of elevation only (Duvall et al., 2012). This allows us to infer the age-elevation relation of source catchment from detrital ages [i.e., for the observed detrital ages t_i (i = 1,2,3…p), we retrieved the elevations z_i (i = 1,2,3…p) in the source area]. The elevation points were sampled by the MCMC (Markov chain Monte Carlo) algorithm (e.g., Avdeev et al., 2011, Duvall et al., 2012). According to each t–z path, the detrital ages can be converted into elevation points, allowing the derivation of its probability distribution function.

For N detrital ages, we assume that these particles are uniformly distributed across the watershed. Therefore, the elevation distribution of these particles should represent a sample chosen from the overall watershed elevation data (i.e., the elevation distribution of the particles and the watershed elevations are assumed to be independent and identically distributed). Consequently, we selected N elevation samples from the watershed and assigned age values to these samples based on their elevation in increasing order, thus obtaining the age-elevation curve. To determine whether the CDF (cumulative probability function) of these chosen points matches that of the source catchment hypsometry, we turned to the two-sample Kuiper test that is (relatively to the Kolmogorov-Smirnov test) insensitive to the tails of the distribution and guarantees equal sensitivities to all variable values (Kuiper, 1962; Vermeesch, 2007). We used the Kuiper test at the 95% significance level (Ruhl et al., 2005; Vermeesch, 2007) and chose the most proper *t–z* path that the best collapse the CDF of the source catchment. Accordingly, the slope of the *t–z* path is the erosion rates of the source area. We choose the last stage slope of the *t–z* path as the million-year erosion rates. Because the monotonic positive thermochronological age-elevation relationship assumption is not valid for the Chindwin basin, the western margin of which consists of a thrust belt (the Kabaw Fault in Figure 1b, Burma Earth Sciences Research Division, 1977), we applied this approach only to the upper Ayeyarwady catchment.

3.4. ^{10}Be-derived basin-averaged erosion rates at thousand-year timescales

Quartz grains were separated from the 125-500 μm size window of nine sand samples following standard magnetic, heavy-liquid, and acid dissolution procedures at the University of Melbourne (Schaefer et al., 2022). The ^{10}Be concentrations were then measured by accelerator mass spectrometry (AMS) at the Australian National University. Erosion rates were calculated according to Zhang et al. (2017). In a steadily eroding landscape with rock density ρ_r (calculated according to point-counting data), the catchment-averaged erosion rate (ε) is:

$$\varepsilon = (P_{avg}\Lambda) / (N\rho_r) \quad (1)$$

where N is the ^{10}Be concentration in sediment, P_{avg} is the average production rate within the catchment, and Λ is the production attenuation scale in rock (~160 g cm^{-2}) (Lal, 1991). Solving equation (1) for ε requires estimates of P_{avg}. Using the Microsoft Excel calculator *Cosmocalc* (Vermeesch, 2007), we scaled the cosmogenic nuclide production rates for each pixel (~30m × ~30 m) from SRTM-DEM data for both elevation and latitude to obtain the catchment-averaged production rate (Lal, 1991; Stone, 2000). The shielding factor related to catchment topography was calculated with the algorithm of Codilean (2006). Results are reported in Supporting Information S2, Tables S6.

3.5. Calculation of present-day erosion rates

Present-day erosion rates can be directly calculated from sediment fluxes, catchment areas, and average density of source rocks (SRD index obtained from quantitative mineralogical data in the absence of hydraulic-sorting effects; Garzanti and Andò, 2007). For sub-catchments where gauging data were not available, we partitioned gauged sediment fluxes in the mainstem by forward mixing modeling based on integrated petrographic and heavy-mineral data (Garzanti et al., 2012). The forward mixing model assumes that the compositional signature of detritus derived from each end-member source is known accurately, then the relative amount of sediment contributed by diverse tributaries or distinct geological domains (endmembers) can be quantitatively assessed by independent forward-mixing calculations. For each river basin, the composition of detritus (petrography and heavy minerals) derived exclusively from each single geological unit was considered as an endmember.

After the relative contributions from different parent sources (e.g., catchments) to a daughter sediment were calculated using the mixing model, they are partitioned among the different sources according to the sediment flux (Mt/a), and a sediment budget is obtained. The average density (g/cm^3) of the exposed source rocks was calculated according to sand mineralogy (SRD index of Garzanti and Andò, 2007). Erosion rates for each source (mm/a) can be finally calculated as the ratio between the sediment yield and the average density of exposed rocks (g/cm^3). Detailed method, rationale, and endmember choices for forward mixing modeling are described in full in Supporting Information S1, Text S2. The sediment yield is the sum of bedload and suspended load normalized by dividing by the upstream drainage area. Bedload fluxes were adopted from literature modelling data calculated using the *WBMsed* model (Cohen et al., 2022).

4. Results

4.1. Petrography and heavy minerals

Upper Ayeyarwady sand is feldspatho-quartzose with plagioclase > K-feldspar, minor phyllite, schist, and felsitic volcanic rock fragments, and abundant mica (mostly biotite). The rich transparent-heavy-mineral (tHM) suite is dominated by hornblende and epidote, with minor garnet, pyroxene, kyanite, and Cr-spinel (Figure 2). The Chindwin River, by contrast, carries feldspatho-litho-quartzose sand with more quartz and lithic fragments (shale, sandstone, chert, felsitic and microlitic volcanic, phyllite/schist, and serpentine-schist types), and less mica. The moderately rich tHM suite consists of amphibole, clinopyroxene and epidote, with subordinate garnet, kyanite, minor zircon, rutile, enstatite, and rare apatite.

The Mu River draining the CMB and the Wuntho-Popa Arc carries litho-feldspatho-quartzose sand with abundant felsitic volcanic and sedimentary rock fragments, and rare metamorphic rock fragments. The moderately poor tHM suite includes mainly amphibole and epidote, with subordinate garnet, kyanite, pyroxene, and minor zircon, rutile, and apatite. The Yaw River draining the IBR and CMB carries feldspatho-litho-quartzose sand with plagioclase ≈ K-feldspar. Felsitic volcanic and metavolcanic, shale, sandstone, and chert rock fragments are common; mica is rare. The moderately rich, amphibole-dominated tHM suite includes clinopyroxene, epidote, garnet, and minor zircon, titanite, and apatite.

Lower Ayeyarwady feldspatho-litho-quartzose sand is compositionally similar as Chindwin sand (Figure 2) and contains more plagioclase than K-feldspar, mainly pelite, sandstone, slate, phyllite, schist, felsic volcanic, and minor serpentinite-schist lithics, and common mica (mostly biotite). The moderately rich tHM suite mainly consists of amphibole and epidote, with garnet, pyroxene, and minor kyanite, Cr-spinel, zircon, titanite, and apatite.

4.2. Detrital AFT results

The Upper Ayeyarwady is characterized by notably younger detrital AFT ages than the Chindwin River (Figure 3), consistent with thermochronological ages of bedrock sources (Figure 1e). In the Upper Ayeyarwady (samples A, B, C, D), single-grain AFT ages range from 538 Ma to 1.8 Ma, with the main peak at ~9 Ma (Figure 3; Supporting Information S2, Tables S5). More than 90% of the grains are younger than 30 Ma, half being younger than 10 Ma.

In the Upper Chindwin River, detrital AFT ages (samples L and G) range from 549 to 3.2 Ma, with major peaks around 10 Ma and 19 Ma, and minor peaks at 33, 59, and 77 Ma. About one-third of the ages are younger than 15 Ma and another third older than 30 Ma. A similar distribution of AFT ages, ranging from 84.4 to 4.4 Ma with the main peak at ~19 Ma and minor peaks at ~28, ~40, and ~58 Ma, characterizes the Yaw River in the south (sample H; Figure 3). Apatite in the Myitha River (sample M) yielded even older ages, with the main peak at ~19 Ma. A similar distribution of AFT ages, ranging from 97.5 to 7.1 Ma, with the main peak at ~16 Ma and a minor peak at ~30 Ma, characterizes the Mu River (sample E).

The Ayeyarwady River shows more AFT ages older than 20 Ma (~35%) downstream of the Mu confluence (sample F). Downstream of the Chindwin confluence (samples I, J, K, Figure 3), the detrital AFT age distribution becomes similar as that characterizing the Chindwin River, with ages ranging from 127 to 1.4 Ma, the main peak around 13-17 Ma and minor older peaks.

4.3. Million-year timescale erosion rates

Erosion rates at the million-year timescale of Upper Ayeyarwady catchments were obtained through numerical inversion of detrital AFT ages. Since the Chindwin River, draining the IMR, has the bimodal detrital AFT signature, which reflects the activations of different sub-units of IMR (the 19 Ma population from the Paleogene IBR and the 10 Ma population from the IMR core according to Najman et al., 2020, 2022). We only applied inversion modeling method on two small Ayeyarwady tributaries (samples A, B), and two Upper Ayeyarwady samples C and D (see Figure 1b).

The Nmai sub-catchment exhibits the highest rate ($0.34^{+0.04}_{-0.03}$ mm/a; Figures 4a), followed by the Mali sub-catchment (0.10 ± 0.01 mm/a; Figures 4b). Lower rates are inferred for the Upper Ayeyarwady mainstream (0.06-0.07 mm/a; Figures 4c and 4d).

4.4. ^{10}Be results

The ^{10}Be concentration in quartz grains across the Ayeyarwady catchment ranges from $(2.9 \pm 1.0)\times10^4$ atoms/g to $(15.2 \pm 3.0)\times10^4$ atoms/g, with highest values recorded in the Upper Chindwin (Supporting Information S2, Tables S6). As for AFT data, ^{10}Be-derived erosion rates (Figure 5) indicate higher denudation in the Upper Ayeyarwady (from 0.06 mm/a to 0.26 ± 0.06 mm/a) than in the Chindwin catchment (from 0.02 ± 0.005 mm/a to 0.12 ± 0.04 mm/a), with highest rates in the Nmai (0.26 ± 0.06 mm/a) and Mali catchments (0.12 ± 0.03 mm/a) and lowest rates in the Upper Chindwin (0.02 ± 0.005 mm/a) and Mu catchments (0.05 ± 0.01 mm/a) (Figures 5, 6b). The ^{10}Be-derived basin-wide erosion rate calculated here for the entire Ayeyarwady (0.10 ± 0.03 mm/a) is slightly lower than a previous ^{10}Be-derived estimate (0.19 ± 0.03 mm/a) (Wittmann et al., 2020), and much lower than the neighboring Brahmaputra (1.0-1.1 mm/a) (Lupker et al., 2017) and Ganga rivers (0.7-1.2 mm/a) (Lupker et al., 2012) draining the Himalayan Range (Figures 5, 6b).

5. Discussion

5.1. Long-term natural erosion rates

Natural erosion rates at the million-year and thousand-year timescales are broadly consistent in the Upper Ayeyarwady catchment (0.06-0.34 mm/a *vs.* 0.06-0.24 mm/a). Within this catchment, the Mali and Nmai drainages have the highest erosion rates at both million-year (0.10-0.34 mm/a) and thousand-year timescales (0.12-0.26 mm/a). The Upper Ayeyarwady exhibits higher rates than the Upper Chindwin catchment in thousand-year timescale, as indicated by ^{10}Be data (0.06-0.26 mm/a *vs.* 0.02 ± 0.005

mm/a) (Figures 5, 6a, and 6b). The erosion rate in the Upper Chindwin catchment is the lowest (0.02 mm/a) of all locations studied at the thousand-year timescale, while the Lower Chindwin shows higher erosion rates (0.12 mm/a).

These spatial variations in the long-term erosion rates show no significant—and even a slightly negative—correlation with lithological erodibility ($p = 0.08$, Figure 7c), indicating that high sediment fluxes cannot be entirely related to source-rock erodibility as previously hypothesized (Garzanti et al., 2016). However, the erosion rates can be adequately explained by climate, topography and tectonics. Long-term natural erosion rates exhibit a positive correlation with catchment-averaged precipitation ($R^2 = 0.46$, $p = 0.01$, Figure 7b). They also show a weak positive correlation with drainage area weighted average k_{sn} values of bedrock rivers ($R^2 = 0.34$, $p = 0.1$, Figure 7a; river morphometry analysis is provided in Supporting Information S1, Text S1 and results are listed in Supporting Information S2, Table S8), intimately associated with topography and regional tectonics. Our calculated timing and extents of erosion are compatible with the tectonic history of the region. The Mogok Metamorphic Belt, located in the northeastern part of the Irrawaddy catchment (represented by the Nmai and Mali rivers), has experienced exhumation in the Late Oligo-Miocene as determined from mica Ar-Ar dating (Bertrand et al., 2001). This is consistent with the timing of exhumation shown for the region of the Mali River catchment as determined through inversion modelling of our detrital AFT data (Fig 4b, increase from 0.03 to 0.10 mm/a at 24 Ma). Little low temperature thermochronological data are published for the region. However, Lei et al., (2006) show apatite fission track data from adjacent Yunnan that may be consistent with the younger rapid exhumation we calculate through inversion modelling of our detrital AFT data from the Nmai catchment (increase from 0.14- to 0.34 mm/a) at 9.9 Ma (Figures 4a, 6a). By contrast, the Chindwin catchment lies outwith the region of the Mogok Metamorphic Belt, and the lower ^{10}Be-derived thousand-year erosion rates of the upper Chindwin reflect this. The higher values of the lower Chindwin likely reflect input from the Myitha River draining the western Indo-

Myanmar Ranges (erosion rates in thousand-year timescale 0.11 mm/a; Figure 6b), although it has previously been calculated that this river only contributes 5% of sediment to the modern Chindwin River (Garzanti et al., 2016).

5.2. Present-day erosion rates

The composition of Ayeyarwady sand changes significantly downstream of the Chindwin confluence (Figure 2), indicating prominent sediment supply from the Chindwin River. Forward-mixing calculations based on integrated bulk-petrography and heavy-mineral data indicate that sediment in the Lower Ayeyarwady is contributed 38±6% by the Upper Ayeyarwady, 9 ± 7% by the Mu River, and 53 ± 7%, by the Chindwin River. These results are consistent with previously calculated contributions of 45 ± 17% from the Upper Ayeyarwady and of 55 ± 17% from the Chindwin River (Garzanti et al., 2016). The Myitha River is estimated to supply only ~5% of Chindwin River sediments, and the Yaw River to make negligible contributions to the Lower Ayeyarwady.

The suspended sediment flux calculated using forward mixing modeling is similar to the gauged sediment flux in the Upper Chindwin (120 ± 9 Mt/a *vs.* 164 ± 51 Mt/a) but higher than the gauged data in the Upper Ayeyarwady (123 ± 40 Mt/a *vs.* 64 ± 5 Mt/a). Additionally, suspended sediment fluxes calculated by forward mixing modelling are coherent with *WBMed* modeling results (Cohen et al., 2022), indicating that our calculations are reliable (Supporting Information S2, Tables S7).

Present-day erosion rates thus calculated are 0.19 ± 0.02 mm/a for the Upper Ayeyarwady, 0.58 ± 0.48 mm/a for the Mu River, 0.63 ± 0.05 mm/a for the Chindwin River upstream of the Myitha confluence, 0.58 ± 0.18 mm/a for the entire Chindwin catchment, and $0.29^{+0.08}_{-0.06}$ mm/a for the entire Ayeyarwady catchment. Similar rates are estimated for the Shweli (0.18 ± 0.05 mm/a) and Taping (0.26 ± 0.03 mm/a) tributaries to the Upper Ayeyarwady (Figures 5, 6c).

5.3. Present-day vs. long-term natural erosion rates

In the Upper Ayeyarwady catchment, the long-term natural erosion rates at million-year and thousand-year timescales are broadly consistent (Figure 7e), but for the entire Ayeyarwady catchment, present-day erosion rates have increased drastically and by different degrees in different sub-catchments (Figure 7f). The strongest increase is displayed by the Upper Chindwin catchment, where present-day erosion rates are calculated to have risen by a factor of 32 (from 0.02 ± 0.005 mm/a to 0.63 ± 0.05 mm/a) relative to the long-term erosion rate. An increase by a factor of five is recorded for the entire Chindwin catchment (from 0.12 mm/a to 0.58 mm/a), and by a factor of three for the Upper Ayeyarwady (from 0.06 mm/a to 0.19 mm/a). The present-day rate trebled also for the entire Ayeyarwady ($0.29^{+0.08}_{-0.06}$ mm/a) compared to the ^{10}Be-derived long-term rate (0.10 ± 0.03 mm/a) (Figures 5, 6b, 6c). Most noteworthy, present-day erosion rates are three times higher in the Upper Chindwin (0.63 ± 0.05 mm/a) compared to the Upper Ayeyarwady (0.19 ± 0.02 mm/a), marking a clear reversal compared to long-term erosion patterns (Figures 5, 6b, 6c).

Thus, in contrast with the long-term erosion patterns, the Chindwin River has presently replaced the Upper Ayeyarwady as the major sediment contributor to the Lower Ayeyarwady. Whilst we acknowledge that different approaches have been used to calculate the erosion rates over the different timescales, we do not consider that differences of approach can explain the variation we record. Different approaches have been used over various time scales to calculate erosion in fluvial catchments in the Himalaya, and they show little variability between long-term and present-day erosion rates (Lenard et al., 2020; Vance et al., 2003). Furthermore, large basins exhibit broad similarity in sediment discharge recorded by the gauge-derived and cosmogenic radionuclide-derived sediment loads from global compilations of literature data (Covault et al., 2013; Wittmann et al., 2020). This suggests that erosion rates across different timescales can be comparable in active orogens like the Ayeyarwady catchment. For instance, in the adjacent Ganges-Brahmaputra (983.9 ± 209 vs. 1037

Mt/a) and Mekong (54.8 ± 6.4 vs. 78 Mt/a) systems—located west and east of the Ayeyarwady, respectively—cosmogenic and gauge-derived sediment loads show close agreement (Wittmann et al., 2020). Thus we consider that the variations we record are not an artefact of the different measuring approaches we use for different timescales.

This inversion in the scale of erosion between the Chindwin and Upper Ayeyarwady catchment cannot be ascribed to climatic factors, because present-day erosion rates do not significantly correlate with precipitation (p = 0.59, Figure 7d). Moreover, the source-rock lithologies likely remained broadly unchanged over this relatively short timescale, indicating that lithological differences are not responsible for the sharp increase in present-day sediment fluxes of the Chindwin River. Whilst we cannot totally rule out the potential effects of neotectonics in this poorly-mapped region, we argue below that anthropogenic influence is a major contributing factor.

5.4. Accelerated erosion by anthropogenic activities

Previous research has shown how modern sediment yields may increase by one or even two orders of magnitude relative to long-term cosmogenic-derived sediment yields if river catchments are affected by profound changes in land use (Hewawasam, 2003; Vanacker et al., 2007). This appears to be the case for the Ayeyarwady catchment, and here we emphasize that anthropogenic activities represent an important factor driving the sharp recent acceleration in sediment production.

Firstly, alluvial mining, which is affecting no less than one-third of the river length in Myanmar (Figure 6c, Dethier et al., 2023; Shrestha et al., 2020). Satellite imagery reveals that mining areas in Myanmar have expanded rapidly over the last 13 years (Connette et al., 2016). Landsat data from 1985 to 2020 reveal that mining has significantly increased suspended sediment concentrations (SSC) in 23 trunk and tributary rivers of the Chindwin and Upper Ayeyarwady (Dethier et al., 2023; Supporting Information S1, Figure S1). Notably, SSC in the Chindwin River has risen more than tenfold, with the Uyu River—an eastern tributary—experiencing increases of over two orders of magnitude relative to pre-mining levels (Figure 8; Figures S2-S3).

Sediment fluxes and present-day erosion rates correlate strongly with the proportion of land impacted by mining (Figures 9a and 9b). Alluvial mining is most widespread in the Upper Chindwin catchment, which also shows the greatest increase in sediment discharge. Mining-affected areas in the Upper Chindwin (16‰, ~1869 km^2) far exceeds those in the Upper Ayeyarwady (1‰, ~74 km^2); correspondingly, present-day erosion rates are three times higher in the Upper Chindwin River (0.63 ± 0.05 mm/a) than in the Upper Ayeyarwady (0.19 ± 0.02 mm/a) (Figures 6c, 9a-9b).

Secondly, additional anthropogenic factors likely also contributed to enhanced erosion rates. Forest loss has been particularly severe in the Lower Ayeyarwady and delta regions due to cropland expansion, with mean annual deforestation rates reaching 1–2% (Table 1, Figures S4d). In the Upper Chindwin and Upper Ayeyarwady catchments, forest cover has declined by 21% and 23%, respectively (Table 1; Supporting Information S1, Figures S4a-S4d), potentially contributing to the observed sediment flux increases in similar trend. However, the increase in sediment flux in the Upper Chindwin (~30-fold) far exceeds that of the Upper Ayeyarwady (~3-fold), indicating that deforestation alone cannot account for the difference. In the Chindwin, mining activity—often linked to deforestation itself—likely plays a dominant role (Figures S4d, S5d–S5e; McGinn et al., 2021). Other land-use changes, such as settlement expansion, have also contributed to landscape disturbance. Conversely, agricultural land use likely does not explain the increase in Chindwin sediment fluxes, as cultivated area decreased by ~20% between 1999 and 2019 (Table 1). Agriculture is more concentrated in the central and lower plains, including the Mu River basin and Lower Ayeyarwady (Li et al., 2024), and may instead contribute to sediment increases there.

Thirdly, climatic factors such as increased precipitation and temperature—linked, at least in part, to 20th-century global warming—may further enhance erosion in all Ayeyarwady sub-catchments. Between 1981 and 2015, both parameters rose across the Ayeyarwady catchment (Sein et al., 2018), while Southeast Asia experienced more frequent extreme monsoon floods (Loo et al., 2015). These climatic trends may have amplified sediment fluxes in both the Upper Ayeyarwady and Chindwin.

Other anthropogenic influences appear limited. Large dams are absent from the main Ayeyarwady, and only small dams exist on select tributaries, suggesting minimal hydrological disruption from damming (Schmitt et al., 2021).

In summary, alluvial mining is the primary driver of elevated sediment fluxes in the Upper Chindwin, with deforestation providing additional impact. In the Upper Ayeyarwady, both deforestation and mining contribute to increased sediment yields. In contrast, cropland expansion and associated deforestation are the main factors behind increased sediment fluxes in the Lower Ayeyarwady. Intensifying precipitation and more frequent monsoon floods may further augment sediment flux across all sub-catchments. The rapid acceleration in anthropogenic-related erosional processes greatly increased the concentration of suspended sediment (Dethier et al., 2020), resulting in degraded water quality and threats to the life cycles of riverine and riparian flora and fauna (Azevedo-Santos et al., 2021; Keovilignavong, 2019) and to natural equilibria as far as the Ayeyarwady Delta (Chen et al., 2020).

6. Conclusions

Long-term natural erosion rates calculated from apatite fission-track ages and ^{10}Be concentration in quartz grains were much higher in the Upper Ayeyarwady (0.06-0.34 mm/a) than in the Upper Chindwin (0.02 ± 0.005 mm/a) derived by ^{10}Be and controlled by tectonic forcing and climate. Gauged sediment fluxes testify to a drastically different modern scenario. Present-day erosion rates have increased by more than an order of magnitude in the Upper Chindwin and Mu catchments, enough to reverse erosion patterns: despite a three-fold increase in the Upper Ayeyarwady, erosion is now notably faster in the Upper Chindwin (0.63 ± 0. 05 mm/a) than in the Upper Ayeyarwady (0.19 ± 0.02 mm/a). Such a recent drastic change in erosion patterns underscores a profound impact by anthropogenic activities, and especially by extensive alluvial mining for jade and gold in the Upper Chindwin catchment. The expansion of land use related deforestation, and global warming in the 20th century increasing in precipitation and extreme flooding events likely also contributed to increased sediment fluxes in both the Chindwin and Upper Ayeyarwady catchments. Accelerated erosion and consequently increased sediment yield by anthropogenic activities have reduced water quality and changed the natural equilibrium in the Ayeyarwady delta.

Open Research

Data sets from this research are provided in the Supporting Information S2. The supporting data for this study can also be freely accessed on the figshare repository (Dong et al., 2025).

Acknowledgements

We are deeply grateful to the Editor Mikael Attal, to three anonymous reviewers, and to the handling Associate Editor for their constructive comments and helpful suggestions. We thank Xu Ying in Nanjing Hongchuang Geological Service Co., Ltd. for apatite separation, and Yizhou Wang and Edward R. Sobel for help with detrital AFT inversion modeling and data interpretation. We are also grateful to Fei Liu and Nyanmin Naing for sampling in the field, and to Abaz Alimanovic and Keith Fifield for ^{10}Be cosmogenic analysis. This study was financially supported by the Second Tibetan Plateau Scientific Expedition and Research Program (STEP, Grant No. 2019QZKK0204) and National Natural Science Foundation of China (No. 42272111).

Figure Captions

Figure 1. The Ayeyarwady drainage basin. a) Suspended sediment flux of large Asian rivers: Ayeyarwady (2017-2019, Baronas et al., 2020); Mekong (1993-2018, Sok et al., 2021); Ganges-Brahmaputra (pre-1990, Islam et al., 1999); Salween (2017-2019, Baronas et al., 2020); Yangtze (2021, Chinese Hydrological Yearbooks 2021); Yellow

River (2021, Chinese Hydrological Yearbooks 2021); Indus (1993-2003, Inam et al., 2007); Red River (2000-2008, Dang et al., 2010); Pearl River (2021, Chinese Hydrological Yearbooks 2021). b) Geological map and sampling sites (modified from Geological Map of Myanmar, 1977; scale 1:1,500,000). c) Gauge station precipitation data derived spatial distribution of annual precipitation between 2001 and 2010 after Sirisena et al., (2018). d) Channel steepness (k_{sn}). River morphometry analysis is provided in Supporting Information S1, Text S1. e) Bedrock thermochronology from literature data (sources of original data are compiled in Supporting Information S2, Tables S9). AFT-apatite fission track; AHe-apatite (U-Th)/He; ZFT-zircon fission track; ZHe-zircon (U-Th)/He.

Figure 2. Petrographic composition and heavy-mineral suites of Ayeyarwady River sands. Q = quartz; F = feldspars; L = lithic fragments (Lv = volcanic; Lm = metamorphic; Ls = sedimentary, compositional fields after Garzanti et al., 2016); Amp = amphibole; Grt = garnet; Ep = epidote-group; ZTR = zircon + tourmaline + rutile; Px = pyroxene; Ol = olivine; Sp = Cr-spinel; Cld = chloritoid; St = staurolite; And = andalusite; Ky = kyanite; Sil = sillimanite. Grey shaded ovals indicate the cluster of Lower Ayeyarwady. Capital letters refer to sample sites (see Fig 1b).

Figure 3. Kernel Density Estimates of measured AFT age distributions plotted with *DensityPlotter* (Vermeesch, 2012). Pie charts represent relative abundances of different age groups (see legend).

Figure 4. Numerical modeling results. Bedrock exhumation history is derived from detrital AFT data under different erosion models.

Figure 5. Comparison of erosion rates at different timescales.

Figure 6. Erosion rate maps of the Ayeyarwady drainage at different timescales. a) million-year timescale rate based on detrital AFT numerical modeling; b) thousand-year timescale rate based on ^{10}Be concentration in quartz grains; c) present-day rate based on gauged sediment fluxes combined with forward mixing modeling. Remote

sensing data on alluvial mining (Maus et al., 2022) and mining-affected drainages (Dethier et al., 2023) are highlighted in red. Sources of gauged sediment data: Upper Chindwin at Kalewa (1991-2010) (Sirisena et al., 2021); Upper Ayeyarwady at Sagaing (1990-2010, IFC, 2017); Upper Shweli and Upper Taping from Chinese Hydrological Yearbooks (1958-1987).

Figure 7. Correlations between erosion rates at different timescales and their potential controls with 95% confidence band in grey. (a-b) Long-term natural erosion rates *versus* catchment-average k_{sn} and precipitation. (c) Long-term natural erosion rates *versus* lithological erodibility (rock erodibility index from Moosdorf et al., 2018). (d) Present-day erosion rate *versus* precipitation. (e) ^{10}Be-derived *versus* AFT-derived erosion rates. (f) ^{10}Be-derived *versus* present-day erosion rates (capital letters in key denote sample sites as per Fig 1b).

Figure 8. Expansion of river mining activities has led to increased suspended sediment concentration in the Chindwin and Uyu rivers. (a) Representative images from Google Earth Pro from 1988. 1998, 2008 and 2020, show expansion of river mining activities in the Uyu River drainage. White arrows show the river direction. White boxes refer to location of data shown in b. (b) Average river true color obtained through Landsat imagery (Landsat 5 and Landsat 7), from 1984 to 2020 in December using the average red-green-blue (RGB) reflectance method (Dethier et al., 2022). The color gradient, ranging from blue to yellow, indicates increasing suspended sediment concentration. The bar numbers in (b) correspond to the locations shown in the first image of (a).

Figure 9. Erosion rates increment positively correlated to the proportion of mining area. (a) Present-day erosion rates increase with the mining area proportion expanding. (b) Erosion rates increment positively correlates with mining area proportion increasing. Erosion rates increment = 100 × (present-day erosion rates - long-term erosion rates) / long-term erosion rates erosion rate.

Table 1. Table 1 Ayeyarwady catchments land use and land cover changes.

References

Adams, B.A., Whipple, K.X., Forte, A.M., Heimsath, A.M., Hodges, K.V. (2020). Climate controls on erosion in tectonically active landscapes. *Science Advances*, *6*, eaaz3166. https://doi.org/10.1126/sciadv.aaz3166

Allen, R., Najman, Y., Carter, A., Parrish, R., Bickle, M., Paul, M. et al. (2008). Provenance of the Tertiary sedi-mentary rocks of the Indo-BurmanRanges, Burma (Myanmar): Burman arc or Himalayan-derived? *Journal of the Geological Society (London)*,*165*, 1045–1057. https://doi.org/10.1144/0016-76492007-143

Andò, S., Garzanti, E. (2014). Raman spectroscopy in heavy-mineral studies. *Geological Society, London, Special Publications*, *386*, 395-412. https://dx.doi.org/10.1144/SP386.2

Avdeev, B., Niemi, N.A., Clark, M.K. (2011). Doing more with less: Bayesian estimation of erosion models with detrital thermochronometric data. *Earth and Planetary Science Letters*, *305*, 385-395. https://doi.org/10.1016/j.epsl.2011.03.020

Azevedo-Santos, V.M., Arcifa, M.S., Brito, M.F.G., Agostinho, A.A., Hughes, R.M., Vitule, J.R.S., Simberloff, D., Olden, J.D., Pelicice, F.M. (2021). Negative impacts of mining on Neotropical freshwater fishes. *Neotropical Ichthyology*, *19*. https://doi.org/10.1590/1982-0224-2021-0001

Barbarand, J., Carter, A., Wood, I., Hurford, T. (2003). Compositional and structural control of fission-track annealing in apatite. *Chemical Geology*, *198*, 107-137. https://doi.org/10.1016/S0009-2541(02)00424-2

Baronas, J.J., Stevenson, E.I., Hackney, C.R., Darby, S.E., Bickle, M.J., Hilton, R.G., Larkin, C.S., Parsons, D.R., Myo Khaing, A., Tipper, E.T. (2020). Integrating Suspended Sediment Flux in Large Alluvial River Channels: Application of a Synoptic Rouse-Based Model to the Irrawaddy and Salween Rivers. *Journal of Geophysical Research: Earth Surface*, 125. https://doi.org/10.1029/2020JF005554

Bender, F. (1983). Geology of Burma. Bontraeger, Berlin.

Best, J. (2018). Anthropogenic stresses on the world's big rivers. *Nature Geoscience*, *12*, 7-21. https://doi.org/10.1038/s41561-018-0262-x

Betka, P.M., Seeber, L., Thomson, S.N., Steckler, M.S., Sincavage, R., Zoramthara, C. (2018). Slip-partitioning above a shallow, weak decollement beneath the Indo-Burman accretionary prism. *Earth and Planetary Science Letters*, *503*, 17–28. https://doi.org/10.1016/j.epsl.2018.09.003

Brewer, I. D., Burbank, D. W., & Hodges, K. V. (2003). Modeling detrital cooling-age populations: Insights from two Himalayan catchments. *Basin Research*, *15*, 305–320. https://doi.org/10.1046/j.1365-2117.2003.00211.x

Brunnschweiler, R. O. (1966). On the geology of the Indoburman ranges. *Journal of the Geological Society of Australia*, *13*(1), 137-194. https://doi.org/10.1080/00167616608728608

Burma Earth Sciences Research Division (1977). Geological Map of the Socialist Republic of the Union of Burma, 1:1000000. *Security Printing Works, Burma*.

Chen, D., Li, X., Saito, Y., Liu, J.P., Duan, Y., Liu, S.a., Zhang, L. (2020). Recent evolution of the Irrawaddy (Ayeyarwady) Delta and the impacts of anthropogenic activities: A review and remote sensing survey. *Geomorphology*, *365*. https://doi.org/10.1016/j.geomorph.2020.107231

Codilean, A.T. (2006). Calculation of the cosmogenic nuclide production topographic shielding scaling factor for large areas using DEMs. *Earth Surface Processes and Landforms*, *31*, 785-794. https://doi.org/10.1002/esp.1336

Cohen, S., Syvitski, J., Ashley, T., Lammers, R., Fekete, B., Li, H.Y. (2022). Spatial Trends and Drivers of Bedload and Suspended Sediment Fluxes in Global Rivers. *Water Resources Research*, *58*. https://doi.org/10.1029/2021WR031583

Connette, K. L., Connette, G., Bernd, A., Phyo, P., Aung, K., Tun, Y., et al. (2016). Assessment of Mining Extent and Expansion in Myanmar Based on Freely-Available Satellite Imagery. *Remote Sensing*, *8*(11). https://doi.org/10.3390/rs8110912

Covault, J.A., Craddock, W.H., Romans, B.W., Fildani, A., Gosai, M. (2013). Spatial and Temporal Variations in Landscape Evolution: Historic and Longer-Term Sediment Flux through Global Catchments. *The Journal of Geology*, *121*, 35-56. https://doi.org/10.1086/668680

Dang, T.H., Coynel, A., Orange, D., Blanc, G., Etcheber, H., Le, L.A. (2010). Long-term monitoring (1960–2008) of the river-sediment transport in the Red River Watershed (Vietnam): Temporal variability and dam-reservoir impact. *Science of The Total Environment*, *408*, 4654-4664. https://doi.org/10.1016/j.scitotenv.2010.07.007

Dethier, E.N., Renshaw, C.E., Magilligan, F.J. (2022). Rapid changes to global river suspended sediment flux by humans. *Science*, *376*, 1447-1452. https://doi.org/10.1126/science.abn798

Dethier, E.N., Silman, M., Leiva, J.D., Alqahtani, S., Fernandez, L.E., Pauca, P., Çamalan, S., Tomhave, P., Magilligan, F.J., Renshaw, C.E., Lutz, D.A. (2023). A global rise in alluvial mining increases sediment load in tropical rivers. *Nature*, *620*, 787-793. https://doi.org/10.1038/s41586-023-06309-9

Dong, X, Hu,X., Li G., Garzanti, E., Najman, Y., Liang, W., Tian, Y., Wang, J. (2025). Dataset for Accelerated erosion and sediment fluxes by anthropogenic mining activities in the Irrawaddy River [Dataset]. *figshare*. https://doi.org/10.6084/m9.figshare.27747153.v9

Duvall, A. R., Clark, M. K., Avdeev, B., Farley, K. A., & Chen, Z. (2012). Widespread late Cenozoic increase in erosion rates across the interior of eastern Tibet constrained by detrital low-temperature thermochronometry. *Tectonics*, *31*, TC3014. https://doi.org/10.1029/2011TC002969

Furuichi, T., Win, Z., Wasson, R.J. (2009). Discharge and suspended sediment transport in the Ayeyarwady River, Myanmar: centennial and decadal changes. *Hydrological Processes*, *23*, 1631-1641. https://doi.org/10.1002/hyp.7295

Gallagher, K., Brown, R.W., and Johnson, C. (1998). Fission track analysis and its applications to geological problems. *Annual Review of Earth and Planetary Sciences*, *26*, 519-572. https://doi.org/10.1146/annurev.earth.26.1.519

Garzanti, E. (2019). *Petrographic classification of sand and sandstone. Earth-Science Reviews*, *192*, 545-563. https://doi.org/10.1016/j.earscirev.2018.12.014

Garzanti, E., Andò, S. (2007). Heavy-mineral concentration in modern sands: implications for provenance interpretation. Mange, M., Wright, D. (Eds.), Heavy Minerals in Use, *Developments in Sedimentology Series*, *58*, 517-545. https://doi.org/10.1016/S0070-4571(07)58020-9

Garzanti, E., Andò, S. (2019). Heavy Minerals for Junior Woodchucks. *Minerals*, *9*, 148. https://doi.org/10.3390/min9030148

Garzanti, E., Resentini, A., Vezzoli, G., Andò, S., Malusà, M., Padoan, M. (2012). Forward compositional modelling of Alpine orogenic sediments. *Sedimentary Geology*, *280*, 149-164. https://doi.org/10.1016/j.sedgeo.2012.03.012

Garzanti, E., Wang, J.-G., Vezzoli, G., Limonta, M. (2016). Tracing provenance and sediment fluxes in the Irrawaddy River basin (Myanmar). *Chemical Geology*, *440*, 73-90. https://doi.org/10.1016/j.chemgeo.2016.06.010

Gemignani, L., van der Beek, P. A., Braun, J., Najman, Y., Bernet, M., Garzanti, E., & Wijbrans, J. R. (2018). Downstream evolution of the thermochronologic age signal in the Brahmaputra catchment (eastern Himalaya): Implications for the detrital record of erosion. *Earth and Planetary Science Letters*, *499*, 48-61. https://doi.org/10.1016/j.epsl.2018.07.019

Gleadow, A.J.W., Gleadow, S.J., Belton, D.X., Kohn, B.P., Krochmal, M.S., Brown, R.W. (2009). Coincidence mapping - a key strategy for the automatic counting of fission tracks in natural minerals. *Geological Society, London, Special Publications*. *324*, 25-36. https://doi.org/10.1144/SP324.2

Gordon, R. (1885). The Irawadi River. *Proceedings of the royal geographical society and monthly record of geography*, *7*, 292-331.

Hasebe, N., Barbarand, J., Jarvis, K., Carter, A., Hurford, A.J. (2004). Apatite fission-track chronometry using laser ablation ICP-MS. *Chemical Geology*, *207*, 135-145. https://doi.org/10.1016/j.chemgeo.2004.01.007

Hewawasam, T., Blanckenburg, F. v., Schaller, M., & Kubik, P. (2003). Increase of human over natural erosion rates in tropical highlands constrained by cosmogenic nuclides. *Geology*, *31*(7), 597-600. https://doi.org/10.1130/0091-7613(2003)031<0597:IOHONE>2.0.CO;2

Inam, A., Clift, P., Giosan, L., Tabrez, A., Tahir, M. (2007). The Geographic, Geological and Oceanographic Setting of the Indus River. *Large Rivers: Geomorphology and Management*, *1*, 333-346. https://doi.org/10.1002/9781119412632.ch17

Ingersoll, R.V., Bullard, T.F., Ford, R.L., Grimm, J.P., Pickle, J.D., Sares, S.W. (1984). The effect of grain size on detrital modes: a test of the Gazzi–Dickinson point-counting method. *Journal of sedimentary Petrology*, *54*, 103-116. https://doi.org/10.1306/212F83B9-2B24-11D7-8648000102C1865D

International Finance Corporation (IFC). (2017). Baseline assessment report: geomorphic and sediment transport. *Strategic Environmental Assessment of the Hydropower Sector in Myanmar*, 1-44.

Islam, M.R., Begum, S.F., Yamaguchi, Y., Ogawa, K. (1999). The Ganges and Brahmaputra rivers in Bangladesh: basin denudation and sedimentation. *Hydrological Processes*, *13*, 2907-2923. https://doi.org/10.1002/(SICI)1099-1085(19991215)13:17<2907::AID-HYP906>3.0.CO;2-E

Jonell, T.N., Giosan, L., Clift, P.D., Carter, A., Bretschneider, L., Hathorne, E.C., Barbarano, M., Garzanti, E., Vezzoli, G., Naing, T. (2022). No modern Irrawaddy River until the late Miocene-Pliocene. *Earth and Planetary Science Letters*, *584*, https://doi.org/10.1016/j.epsl.2022.117516

Keovilignavong, O. (2019). Mining governance dilemma and impacts: A case of gold mining in Phu-Hae, Lao PDR. *Resources Policy*, *61*, 141-150. https://doi.org/10.1016/j.resourpol.2019.02.002

Kubik, T.H.F.v.B.M.S.P. (2003). Increase of human over natural erosion rates in tropical highlands constrained by cosmogenic nuclides. *Geology*, *31*, 597-600. https://doi.org/10.1130/0091-7613(2003)031<0597:IOHONE>2.0.CO;2

Kuiper, N. H. (1962). Tests concerning random points on a circle. *Proceedings of the Koninklijke Nederlandse Akademie van Wetenschappen Series A*, *63*, 38–47.

Kyaw Linn, O., Khin, Z., Meffre, S., Myitta, Day Wa, A., Lai, C.-K. (2015). Provenance of the Eocene sandstones in the southern Chindwin Basin, Myanmar: Implications for the unroofing history of the Cretaceous–Eocene magmatic arc. *Journal of Asian Earth Sciences*, *107*, 172-194. https://doi.org/10.1016/j.jseaes.2015.04.029

Lal, D. (1991). Cosmic ray labeling of erosion surfaces: in situ nuclide production rates and erosion models. *Earth and Planetary Science Letters*, *104*, 424-439. https://doi.org/10.1016/0012-821X(91)90220-C

Lei, Y.L., Ji, J.Q., Gong, D.H., Zhong, D.L., Wang, X.S., Zhang, J., Wang, X.M. (2006). Thermal and denudational history of granitoid batholith recorded by apatite fission track in the Dulong River region in northwestern Yunnan, since Late Miocene. *Acta Petrologica Sinica*, *22*(4), 938-948. https://doi.org/1000-0569/2006/022(04)-0938-48

Lenard, S.J.P., Lavé, J., France-Lanord, C., Aumaître, G., Bourlès, D.L., Keddadouche, K. (2020). Steady erosion rates in the Himalayas through late Cenozoic climatic changes. *Nature Geoscience*, *13*, 448-452. https://doi.org/10.1038/s41561-020-0585-2

Li, R., Li, C., Hou, D., Xing, H., & Zhu, A. X. (2024). Dynamics in Land Cover and Landscape Patterns of Myanmar: A Three-Decade Perspective (1990–2020). *Land*, *13*(12). https://doi.org/10.3390/land13122212

Li, R., Mei, L., Zhu, G., Zhao, R., Xu, X., Zhao, H., et al. (2013). Late mesozoic to cenozoic tectonic events in volcanic arc, West Burma Block: Evidences from U-Pb zircon dating and apatite fission track data of granitoids. *Journal of Earth Science*, *24*(4), 553-568. https://doi.org/10.1007/s12583-013-0349-7

Licht, A., Win, Z., Westerweel, J., Cogné, N., Morley, C. K., Chantraprasert, S., et al. (2020). Magmatic history of central Myanmar and implications for the evolution of the Burma Terrane. *Gondwana Research*, *87*, 303-319. https://doi.org/10.1016/j.gr.2020.06.016

Lindert, P.H. (2000). Shifting Ground: The Changing Agricultural Soils of China and Indonesia. *The Journal of Asian Studies*, *60*, 824-825. https://doi.org/10.7551/mitpress/6212.001.0001

Loo, Y. Y., Billa, L., & Singh, A. (2015). Effect of climate change on seasonal monsoon in Asia and its impact on the variability of monsoon rainfall in Southeast Asia. *Geoscience Frontiers*, *6*(6), 817-823. https://doi.org/10.1016/j.gsf.2014.02.009

Lupker, M., Blard, P.-H., Lavé, J., France-Lanord, C., Leanni, L., Puchol, N., Charreau, J., Bourlès, D. (2012). 10Be-derived Himalayan denudation rates and sediment budgets in the Ganga basin. *Earth and Planetary Science Letters*, *333*, 146-156. https://doi.org/10.1016/j.epsl.2012.04.020

Lupker, M., Lavé, J., France-Lanord, C., Christl, M., Bourlès, D., Carcaillet, J., Maden, C., Wieler, R., Rahman, M., Bezbaruah, D., Xiaohan, L. (2017). 10Be systematics in the Tsangpo-Brahmaputra catchment: the cosmogenic nuclide legacy of the eastern Himalayan syntaxis. *Earth Surface Dynamics*, *5*, 429-449. https://doi.org/10.5194/esurf-5-429-2017

Maus, V., Giljum, S., da Silva, D.M., Gutschlhofer, J., da Rosa, R.P., Luckeneder, S., Gass, S.L.B., Lieber, M., McCallum, I. (2022). An update on global mining land use. *Scientific Data*, *9*, 433. https://doi.org/10.1038/s41597-022-01547-4

McGinn, A. J., Wagner, P. D., Htike, H., Kyu, K. K., & Fohrer, N. (2021). Twenty years of change: Land and water resources in the Chindwin catchment, Myanmar between 1999 and 2019. *Sci Total Environ*, *798*, 148766. https://www.ncbi.nlm.nih.gov/pubmed/34375254

Mitchell, A.H.G. (1993). Cretaceous-Cenozoic tectonic events in the western Myanmar(Burma)-Assam region. *Journal of the Geological Society (London)*, *150*, 1089–1102. https://doi.org/10.1144/gsjgs.150.6.1089

Mitchell, A. H. G., Chung, S.-L., Thura, O., Lin, T.-S., & Hung, C.-H. (2012). Zircon U-Pb ages in Myanmar: Magmatic-metamorphic events and the closure of a Neotethys ocean? Journal of Asian Earth Sciences, 56, 1–23. https://doi.org/10.1016/j.jseaes.2012.04.019

Moosdorf, N., Cohen, S., & von Hagke, C. (2018). A global erodibility index to represent sediment production potential of different rock types. *Applied Geography*, *101*, 36-44. https://doi.org/10.1016/j.apgeog.2018.10.010

Naing, T.T., Bussien, D.A., Winkler, W.H., Nold, M., Von Quadt, A. (2014). Provenance study on Eocene-Miocene sandstones of the Rakhine Coastal Belt, Indo-Burman Ranges of Myanmar: geodynamic implications. *Geological Society, London, Special Publications*, *386*, 195–216. https://doi.org/10.1144/SP386.10

Najman, Y., Sobel, E.R., Millar, I., Luan, X., Zapata, S., Garzanti, E., Parra, M., Vezzoli, G., Zhang, P., Wa Aung, D., Paw, S.M.T.L., Lwin, T.N. (2022). The Timing of Collision Between Asia and the West Burma Terrane, and the Development of the Indo-Burman Ranges. *Tectonics*, *41*. https://doi.org/10.1029/2021TC007057

Najman, Y., Sobel, E.R., Millar, I., Stockli, D.F., Govin, G., Lisker, F., Garzanti, E., Limonta, M., Vezzoli, G., Copley, A., Zhang, P., Szymanski, E., Kahn, A. (2020). The exhumation of the Indo-Burman Ranges, Myanmar. *Earth and Planetary Science Letters*, *530*. https://doi.org/10.1016/j.epsl.2019.115948

Robinson, R.A.J., Bird, M.I., Oo, Nay W., Hoey, T.B., Aye, Maung M., Higgitt, D.L., X. X, L., Swe, A., Tun, T., Win, Swe L. (2007). The Irrawaddy River Sediment Flux to the Indian Ocean: The Original Nineteenth-Century Data Revisited. The *Journal of Geology*, *115*, 629-640. https://doi.org/10.1086/521607

Ruhl, K. W., & Hodges, K. V. (2005). The use of detrital mineral cooling ages to evaluate steady state assumptions in active orogens: An example from the central Nepalese Himalaya. *Tectonics*, *24*, TC4015. https://doi.org/10.1029/2004TC001712

Schaefer, J.M., Codilean, A.T., Willenbring, J.K., Lu, Z.-T., Keisling, B., Fülöp, R.-H., Val, P. (2022). Cosmogenic nuclide techniques. *Nature Reviews Methods Primers*, *2*. https://doi.org/10.1038/s43586-022-00096-9

Schmitt, R. J. P., Kittner, N., Kondolf, G. M., & Kammen, D. M. (2021). Joint strategic energy and river basin planning to reduce dam impacts on rivers in Myanmar. *Environmental Research Letters*, *16*(5). https://doi.org/10.1088/1748-9326/abe329

Sein, K. K., Chidthaisong, A., & Oo, K. L. (2018). Observed Trends and Changes in Temperature and Precipitation Extreme Indices over Myanmar. *Atmosphere*, *9*(12). https://doi.org/10.3390/atmos9120477

Shrestha, S., Gunawardana, S.K., Piman, T., Babel, M.S. (2020). Assessment of the impact of climate change and mining activities on streamflow and selected metal's loading in the Chindwin River, Myanmar. *Environmental Research*, *181*, 108942. https://doi.org/10.1016/j.envres.2019.108942

Sirisena, T.A.J.G., Maskey, S., Bamunawala, J., Ranasinghe, R. (2021). Climate Change and Reservoir Impacts on 21st-Century Streamflow and Fluvial Sediment Loads in the Irrawaddy River, Myanmar. *Frontiers in Earth Science*, *9*. https://doi.org/10.3389/feart.2021.644527

Sirisena, T.A.J.G., Maskey, S., Ranasinghe, R., Babel, M.S. (2018). Effects of different precipitation inputs on streamflow simulation in the Irrawaddy River Basin, Myanmar. *Journal of Hydrology: Regional Studies*, *19*, 265-278. https://doi.org/10.1016/j.ejrh.2018.10.005

Sok, T., Oeurng, C., Kaing, V., Sauvage, S., Kondolf, G.M., Sánchez-Pérez, J.M. (2021). Assessment of suspended sediment load variability in the Tonle Sap and Lower Mekong Rivers, Cambodia. *Catena*, *202*. https://doi.org/10.1016/j.catena.2021.105291

Stone, J.O. (2000). Air pressure and cosmogenic isotope production. *Journal of Geophysical Research: Solid Earth*, *105*, 23753-23759. https://doi.org/10.1029/2000JB900181

Suzuki, H., Maung, M., Aung, A. K., & Takai, M. (2004). Jurassic radiolaria from chert pebbles of the Eocene Pondaung Formation, central Myanmar. *Neues Jahrbuch für Geologie und Paläontologie - Abhandlungen*, *231*(3), 369-393. https://doi.org/10.1127/njgpa/231/2004/369

Syvitski, J.P., Kettner, A. (2011). Sediment flux and the Anthropocene. *Philosophical Transactions of the Roy Society A*, *369*, 957-975. https://doi.org/10.1098/rsta.2010.0329

Vanacker, V., von Blanckenburg, F., Govers, G., Molina, A., Poesen, J., Deckers, J., Kubik, P. (2007). Restoring dense vegetation can slow mountain erosion to near natural benchmark levels. *Geology*, *35*. https://doi.org/10.1130/G23109A.1

Vance, D., Bickle, M., Ivy-Ochs, S., Kubik, P.W. (2003). Erosion and exhumation in the Himalaya from cosmogenic isotope inventories of river sediments. *Earth and Planetary Science Letters*, *206*, 273-288. https://doi.org/10.1016/S0012-821X(02)01102-0

Vermeesch, P. (2012). On the visualisation of detrital age distributions. *Chemical Geology*, *312*, 190-194. https://doi.org/10.1016/j.chemgeo.2012.04.021

Vermeesch, P., 2007. CosmoCalc: An Excel add-in for cosmogenic nuclide calculations. *Geochemistry, Geophysics, Geosystems*, *8*. https://doi.org/10.1029/2006GC001530

Vermeesch, P. (2007). Quantitative geomorphology of the White Mountains (California) using detrital apatite fission track thermochronology. *Journal of Geophysical Research*, *112*, F03004. https://doi.org/10.1029/2006JF000671

Wang, H., Saito, Y., Zhang, Y., Bi, N., Sun, X., & Yang, Z. (2011). Recent changes of sediment flux to the western Pacific Ocean from major rivers in East and Southeast Asia. *Earth-Science Reviews*, *108*(1-2), 80-100. https://doi.org/10.1016/j.earscirev.2011.06.003

Wittmann, H., Oelze, M., Gaillardet, J., Garzanti, E., von Blanckenburg, F. (2020). A global rate of denudation from cosmogenic nuclides in the Earth's largest rivers. *Earth-Science Reviews*, *204*. https://doi.org/10.1016/j.earscirev.2020.103147

Yang, R., Luo, Y., Yang, K., Hong, L., & Zhou, X. (2019). Analysis of forest deforestation and its driving factors in Myanmar from 1988 to 2017.

Sustainability, *11*(11), 3047. https://doi.org/10.3390/su11113047

Ye, Y., Wu, L., Cowgill, E., Tian, Y., Lin, X., Xiao, A., Chen, H. (2022). Long-lagged (~19 Myr) response of accelerated river incision to rock uplift on the northern margin of the Tibetan Plateau. *Earth and Planetary Science Letters*, *591*. https://doi.org/10.1016/j.epsl.2022.117608

Zachos, J., Pagani, M., Sloan, L., Thomas, E., & Billups, K. (2001). Trends, Rhythms, and Aberrations in Global Climate 65 Ma to Present. *Science*, *292*, 686-693. https://doi.org/10.1126/science.105941

Zaw, K., Swe, W., Barber, A. J., Crow, M. J., & Nwe, Y.-Y. (2017). Introduction to the geology of Myanmar. *Geological Society, London, Memoirs*, 48(1), 1–17. https://doi.org/10.1144/M48.1

Zhang, H., Kirby, E., Pitlick, J., Anderson, R.S., Zhang, P. (2017). Characterizing the transient geomorphic response to base-level fall in the northeastern Tibetan Plateau. *Journal of Geophysical Research: Earth Surface*, *122*, 546-572. https://doi.org/10.1002/2015JF003715

Zhuang, G., Najman, Y., Tian, Y., Carter, A., Gemignani, L., Wijbrans, J., Jan, M.Q., Khan, M.A. (2018). Insights into the evolution of the Hindu Kush–Kohistan–Karakoram from modern river sand detrital geo- and thermochronological studies. *Journal of the Geological Society*, *175*, 934-948. https://doi.org/10.1144/jgs2018-007

Supporting Information References

Aitchison, J. (1982). The Statistical Analysis of Compositional Data. *Journal of the Royal Statistical Society Series B: Statistical Methodology*, *44*, 139-160. https://doi.org/10.1111/j.2517-6161.1982.tb01195.x

Clubb, F.J., Mudd, S.M., Schildgen, T.F., van der Beek, P.A., Devrani, R., Sinclair, H.D. (2023). Himalayan valley-floor widths controlled by tectonically driven exhumation. *Nature Geoscience*, *16*, 739-746. https://doi.org/10.1038/s41561-023-01238-8

Dethier, E.N., Silman, M., Leiva, J.D., Alqahtani, S., Fernandez, L.E., Pauca, P., Çamalan, S., Tomhave, P., Magilligan, F.J., Renshaw, C.E., Lutz, D.A. (2023). A global rise in alluvial mining increases sediment load in tropical rivers. *Nature*, *620*, 787-793. https://doi.org/10.1038/s41586-023-06309-9Flint, J.J. (1974).

Flint, J.J. (1974). Stream Gradient as a Function of Order, Magnitude, and Discharge. *Water Resources Research*, *10*, 969 - 973. https://doi.org/10.1029/WR010i005p00969

Gallen, S.F., Wegmann, K.W. (2017). River profile response to normal fault growth and linkage: an example from the Hellenic forearc of south-central Crete, Greece. *Earth Surface Dynamics*, *5*, 161-186. https://doi.org/10.5194/esurf-5-161-2017

Garzanti, E., He, J., Barbarano, M., Resentini, A., Li, C., Yang, L., Yang, S., Wang, H.

(2021). Provenance versus weathering control on sediment composition in tropical monsoonal climate (South China) - 2. Sand petrology and heavy minerals. *Chemical Geology*, *564*. https://doi.org/10.1016/j.chemgeo.2020.119997

Hasebe, N., Barbarand, J., Jarvis, K., Carter, A., Hurford, A.J. (2004). Apatite fission-track chronometry using laser ablation ICP-MS. *Chemical Geology*, *207*, 135-145. https://doi.org/10.1016/j.chemgeo.2004.01.007

Martín-Fernández, J. A., C.B.-V.V.P.-G. (2003). Dealing with Zeros and Missing Values in Compositional Data Sets Using Nonparametric Imputation. *Mathematical Geology*, *35*, 253-278. https://doi.org/10.1023/A:1023866030544

Kirby, E., Whipple, K.X. (2012). Expression of active tectonics in erosional landscapes. *Journal of Structural Geology*, *44*, 54-75. https://doi.org/10.1016/j.jsg.2012.07.009

Kirby, E., K. X. Whipple, W. Q. Tang, and Z. L. Chen (2003), Distribution of active rock uplift along the eastern margin of the Tibetan Plateau: Inferences from bedrock channel longitudinal profiles. *Journal of Geophysical Research*, *108*(B4), 2217, https://doi.org/10.1029/2001JB000861

Li, R., Li, C., Hou, D., Xing, H., & Zhu, A. X. (2024). Dynamics in Land Cover and Landscape Patterns of Myanmar: A Three-Decade Perspective (1990–2020). *Land*, *13*(12). https://doi.org/10.3390/land13122212

Li, Z., Chen, J., Han, M., Li, Y., Cao, C., Song, S., Zhang, Y., Yan, J. (2021). Distribution and evolution of knickpoints along the Layue River, Eastern Himalayan Syntaxis. *Journal of Hydrology*, *603*. https://doi.org/10.1016/j.jhydrol.2021.126915

Liedel, S., Caracciolo, L., Beltrán-Triviño, A., Restrepo, J.C., Ángel, J.D.R., Szczerba, M. (2024). A Quantitative Provenance Analysis (QPA) Approach to Quantify Controls on Sediment Generation and Sediment Flux in the Upper Reaches of the Magdalena River (Colombia): 2. Lithological Control on Contribution to Silt- to Clay-Sized Fractions. J*ournal of Geophysical Research: Earth Surface*, *129*. https://doi.org/10.1029/2023JF007379

McGinn, A. J., Wagner, P. D., Htike, H., Kyu, K. K., & Fohrer, N. (2021). Twenty years of change: Land and water resources in the Chindwin catchment, Myanmar between 1999 and 2019. *Sci Total Environ*, *798*, 148766. https://www.ncbi.nlm.nih.gov/pubmed/34375254

Palomares, M., Arribas, J. (1993). Modern stream sands from compound crystalline sources: Composition and sand generation index. *Processes Controlling the Composition of Clastic Sediments*, 313-322. https://doi.org/10.1130/SPE284-p313

Perron, J.T., Royden, L. (2013). An integral approach to bedrock river profile analysis. *Earth Surface Processes and Landforms*, *38*, 570-576. https://doi.org/10.1002/esp.3302

Resentini, A., Goren, L., Castelltort, S., Garzanti, E. (2017). Partitioning sediment flux by provenance and tracing erosion patterns in Taiwan. *Journal of Geophysical Research: Earth Surface*, *122*, 1430-1454. https://doi.org/10.1002/2016JF004026

Schwanghart, W., Scherler, D. (2014). Short Communication: TopoToolbox 2 – MATLAB-based software for topographic analysis and modeling in Earth surface sciences. *Earth Surface Dynamics*, *2*, 1-7. https://doi.org/10.5194/esurf-2-1-2014

Vezzoli, G., Garzanti, E., Limonta, M., Radeff, G. (2020). Focused erosion at the core of the Greater Caucasus: Sediment generation and dispersal from Mt. Elbrus to the Caspian Sea. *Earth-Science Reviews*, *200*. https://doi.org/10.1016/j.earscirev.2019.102987

Weltje, G.J. (1997). End-member modelling of compositional data: numerical statistical algorithms for solving the explicit mixing problem. *Mathematical Geology*, *29*, 503-549. https://doi.org/10.1007/BF02775085

Whipple, K.X., DiBiase, R.A., Crosby, B.T. (2013). 9.28 Bedrock Rivers, Treatise on *Geomorphology*, 550-573. http://dx.doi.org/10.1016/B978-0-12-374739-6.00254-2

Willett, S.D., McCoy, S.W., Perron, J.T., Goren, L., Chen, C.Y. (2014). Dynamic reorganization of river basins. *Science*, *343*, 1248765. http://dx.doi.org/10.1126/science.1248765

Wobus, C., Whipple, K.X., Kirby, E., Snyder, N., Johnson, J., Spyropolou, K., Crosby, B., Sheehan, D. (2006). Tectonics from topography: Procedures, promise, and pitfalls, Tectonics, Climate, and Landscape Evolution. *Geological Society of America Special Paper, Penrose Conference Series*, *398,*55–74. https://doi.org/10.1130/2006.2398(04)

Yang, R., Luo, Y., Yang, K., Hong, L., & Zhou, X. (2019). Analysis of forest deforestation and its driving factors in Myanmar from 1988 to 2017. *Sustainability*, *11*(11), 3047. https://doi.org/10.3390/su11113047

Yang, R., Willett, S.D., Goren, L. (2015). In situ low-relief landscape formation as a result of river network disruption. *Nature*, *520*, 526-529. https://doi.org/10.1038/nature14354

Figure 1.

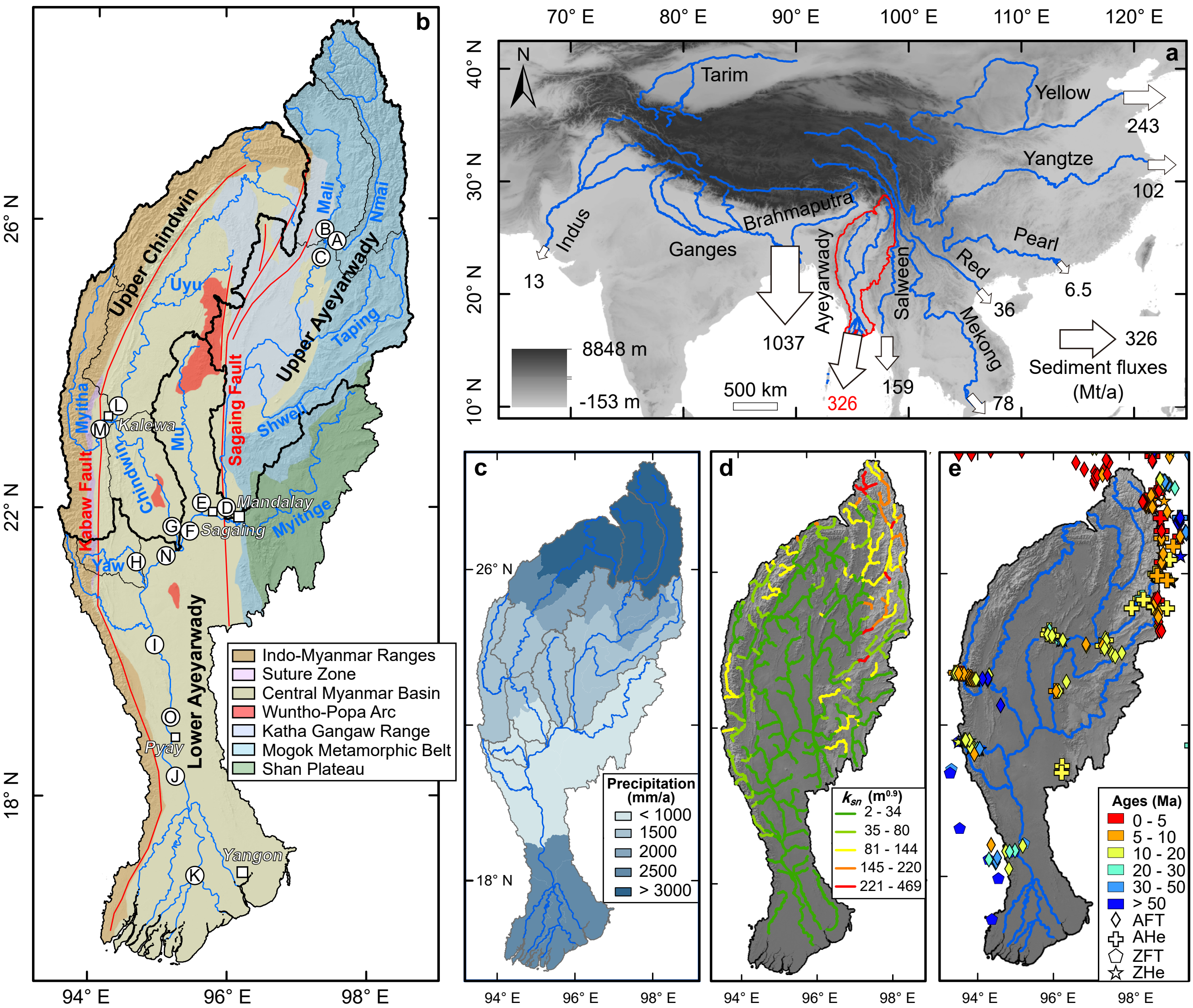

b
26° N
22° N
18° N
94° E
96° E
98° E
Upper Chindwin
Upper Ayeyarwady
Lower Ayeyarwady
Mali
Nmai
Uyu
Taping
Shweli
Myitha
Kalewa
Chindwin
Mu
Sagaing Fault
Kabaw Fault
Mandalay
Sagaing
Myitnge
Yaw
Pyay
Yangon
A
B
C
D
E
F
G
H
I
J
K
L
M
N
O
Indo-Myanmar Ranges
Suture Zone
Central Myanmar Basin
Wuntho-Popa Arc
Katha Gangaw Range
Mogok Metamorphic Belt
Shan Plateau
a
70° E
80° E
90° E
100° E
110° E
120° E
40° N
30° N
20° N
10° N
N
Tarim
Yellow
243
Yangtze
102
Indus
13
Ganges
Brahmaputra
1037
Ayeyarwady
326
Salween
159
Pearl
6.5
Red
36
Mekong
78
8848 m
-153 m
500 km
326
Sediment fluxes (Mt/a)
c
26° N
18° N
Precipitation (mm/a)
< 1000
1500
2000
2500
> 3000
94° E
96° E
98° E
d
k_{sn} ($m^{0.9}$)
2 - 34
35 - 80
81 - 144
145 - 220
221 - 469
e
Ages (Ma)
0 - 5
5 - 10
10 - 20
20 - 30
30 - 50
> 50
AFT
AHe
ZFT
ZHe

Figure 2.

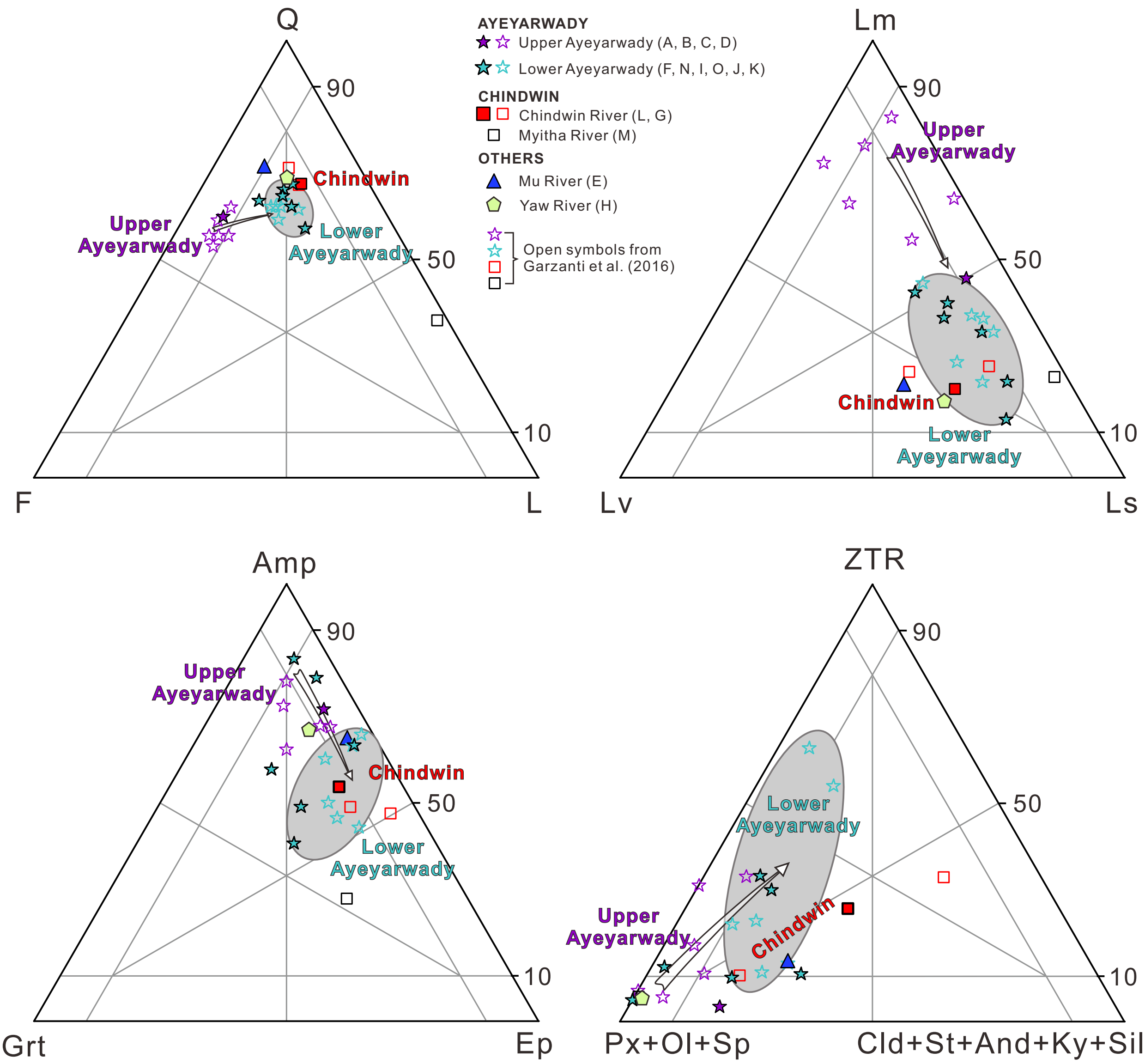
Q
F
L
90
50
10
Chindwin
Upper Ayeyarwady
Lower Ayeyarwady
AYEYARWADY
Upper Ayeyarwady (A, B, C, D)
Lower Ayeyarwady (F, N, I, O, J, K)
CHINDWIN
Chindwin River (L, G)
Myitha River (M)
OTHERS
Mu River (E)
Yaw River (H)
Open symbols from Garzanti et al. (2016)
Lm
Lv
Ls
Amp
Grt
Ep
ZTR
Px+Ol+Sp
Cld+St+And+Ky+Sil

Figure 3.

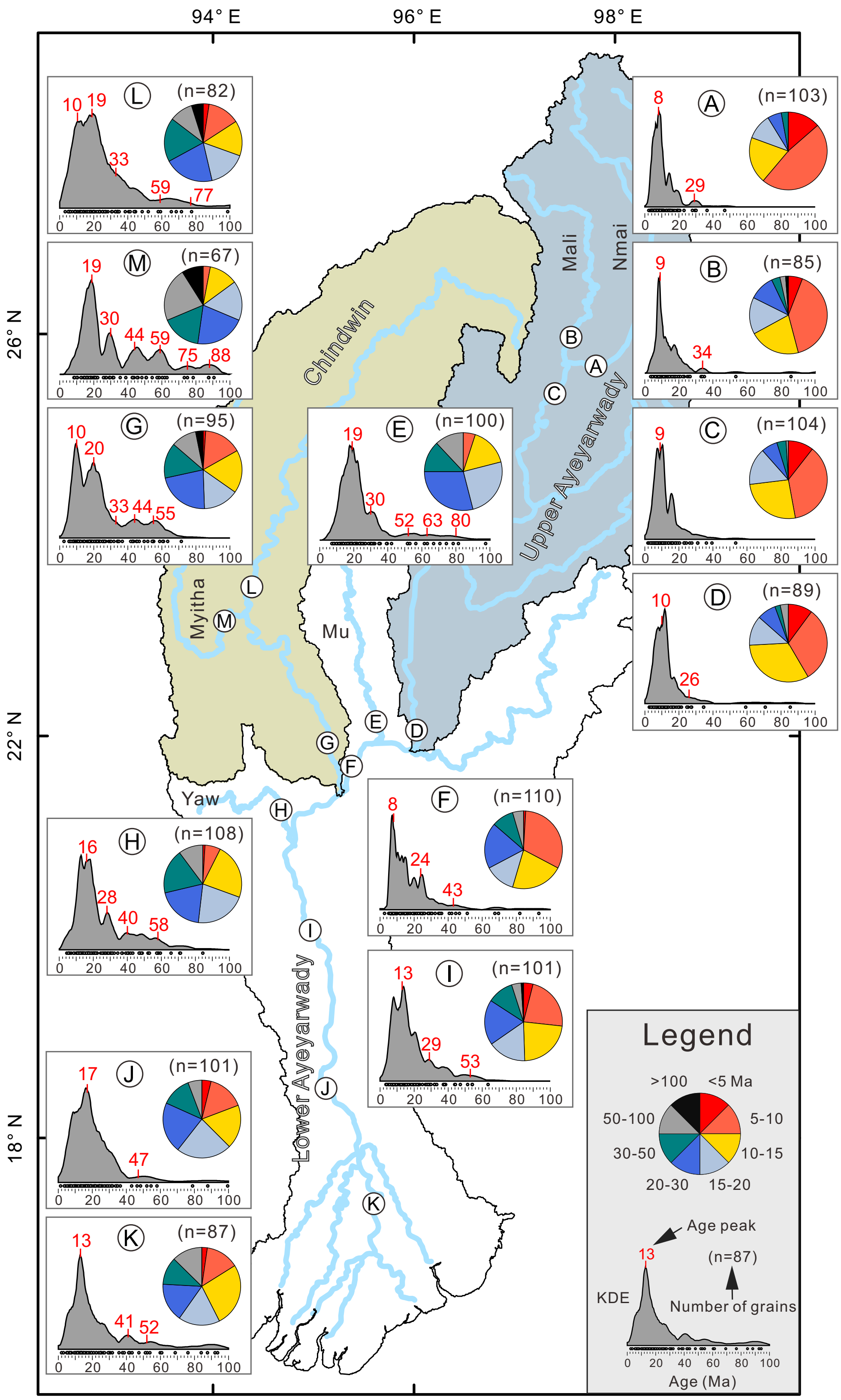

94° E
96° E
98° E
26° N
22° N
18° N
Chindwin
Mali
Nmai
Upper Ayeyarwady
Myitha
Mu
Yaw
Lower Ayeyarwady
Legend
>100
<5 Ma
50-100
5-10
30-50
10-15
20-30
15-20
Age peak
(n=87)
KDE
Number of grains
Age (Ma)

Figure 4.

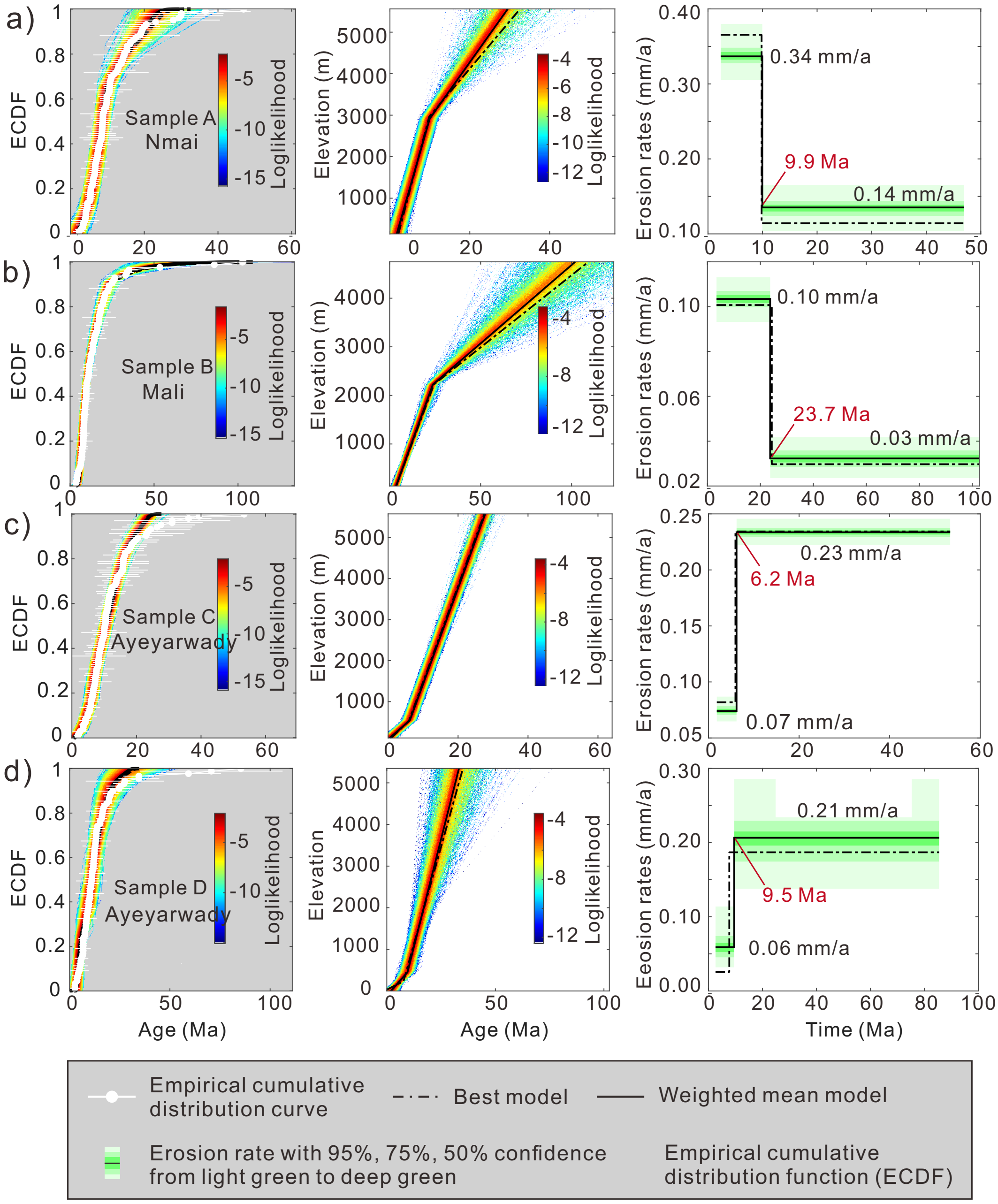

a)
b)
c)
d)
ECDF
Sample A
Nmai
Sample B
Mali
Sample C
Ayeyarwady
Sample D
Ayeyarwady
Loglikelihood
Elevation (m)
Elevation
Erosion rates (mm/a)
Eeosion rates (mm/a)
0.34 mm/a
9.9 Ma
0.14 mm/a
0.10 mm/a
23.7 Ma
0.03 mm/a
0.23 mm/a
6.2 Ma
0.07 mm/a
0.21 mm/a
9.5 Ma
0.06 mm/a
Age (Ma)
Age (Ma)
Time (Ma)
Empirical cumulative distribution curve
Best model
Weighted mean model
Erosion rate with 95%, 75%, 50% confidence from light green to deep green
Empirical cumulative distribution function (ECDF)

Figure 5.

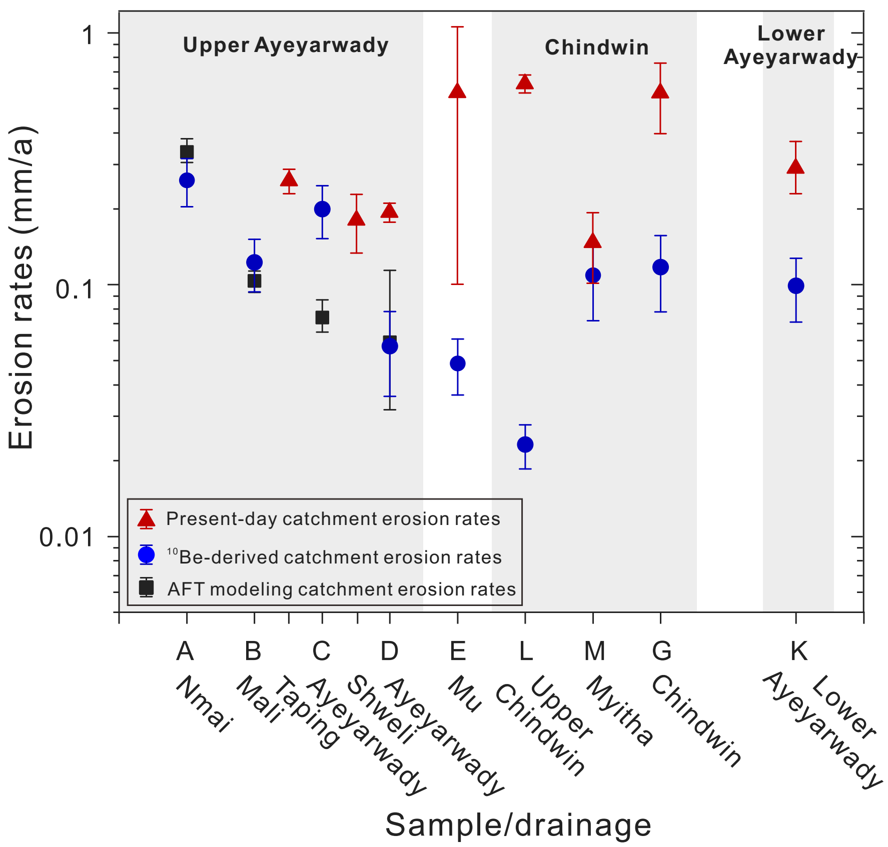

Upper Ayeyarwady
Chindwin
Lower Ayeyarwady
Erosion rates (mm/a)
1
0.1
0.01
Present-day catchment erosion rates
^{10}Be-derived catchment erosion rates
AFT modeling catchment erosion rates
A
B
C
D
E
L
M
G
K
Nmai
Mali
Taping
Ayeyarwady
Shweli
Ayeyarwady
Mu
Upper Chindwin
Myitha
Chindwin
Lower Ayeyarwady
Sample/drainage

Figure 6.

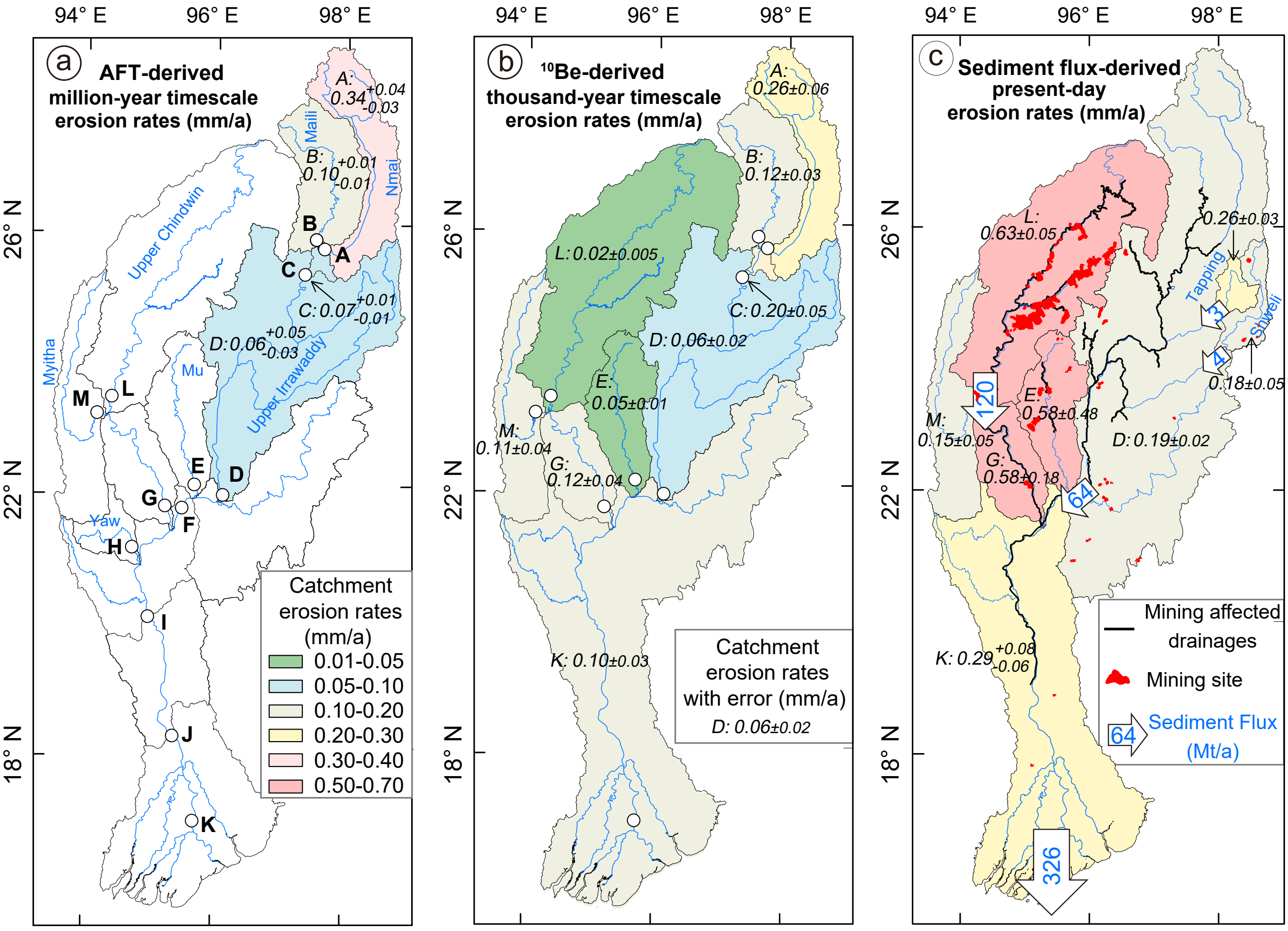

94° E
96° E
98° E
26° N
22° N
18° N
a
AFT-derived
million-year timescale
erosion rates (mm/a)
A: 0.34 +0.04 -0.03
B: 0.10 +0.01 -0.01
C: 0.07 +0.01 -0.01
D: 0.06 +0.05 -0.03
Maili
Nmai
Upper Chindwin
Upper Irrawaddy
Mu
Mytha
Yaw
A
B
C
D
E
F
G
H
I
J
K
L
M
Catchment erosion rates (mm/a)
0.01-0.05
0.05-0.10
0.10-0.20
0.20-0.30
0.30-0.40
0.50-0.70
b
10Be-derived
thousand-year timescale
erosion rates (mm/a)
A: 0.26±0.06
B: 0.12±0.03
C: 0.20±0.05
D: 0.06±0.02
E: 0.05±0.01
L: 0.02±0.005
M: 0.11±0.04
G: 0.12±0.04
K: 0.10±0.03
Catchment erosion rates with error (mm/a)
D: 0.06±0.02
c
Sediment flux-derived
present-day
erosion rates (mm/a)
L: 0.63±0.05
0.26±0.03
Tapping
Shweli
0.18±0.05
3
4
120
M: 0.15±0.05
E: 0.58±0.48
G: 0.58±0.18
D: 0.19±0.02
64
K: 0.29 +0.08 -0.06
326
Mining affected drainages
Mining site
64 Sediment Flux (Mt/a)

Figure 7.

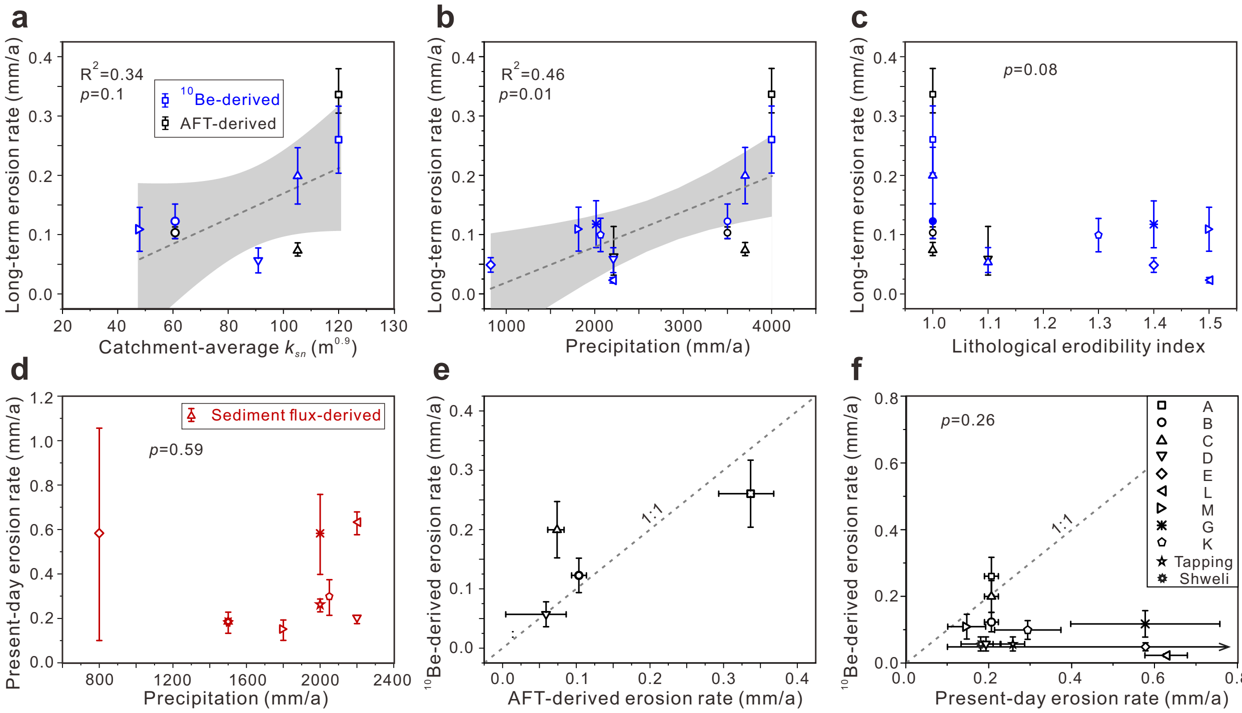

a
R2=0.34
p=0.1
10Be-derived
AFT-derived
Long-term erosion rate (mm/a)
Catchment-average ksn (m0.9)
b
R2=0.46
p=0.01
Long-term erosion rate (mm/a)
Precipitation (mm/a)
c
p=0.08
Long-term erosion rate (mm/a)
Lithological erodibility index
d
Sediment flux-derived
p=0.59
Present-day erosion rate (mm/a)
Precipitation (mm/a)
e
1:1
10Be-derived erosion rate (mm/a)
AFT-derived erosion rate (mm/a)
f
p=0.26
1:1
A
B
C
D
E
L
M
G
K
Tapping
Shweli
10Be-derived erosion rate (mm/a)
Present-day erosion rate (mm/a)

Figure 8.

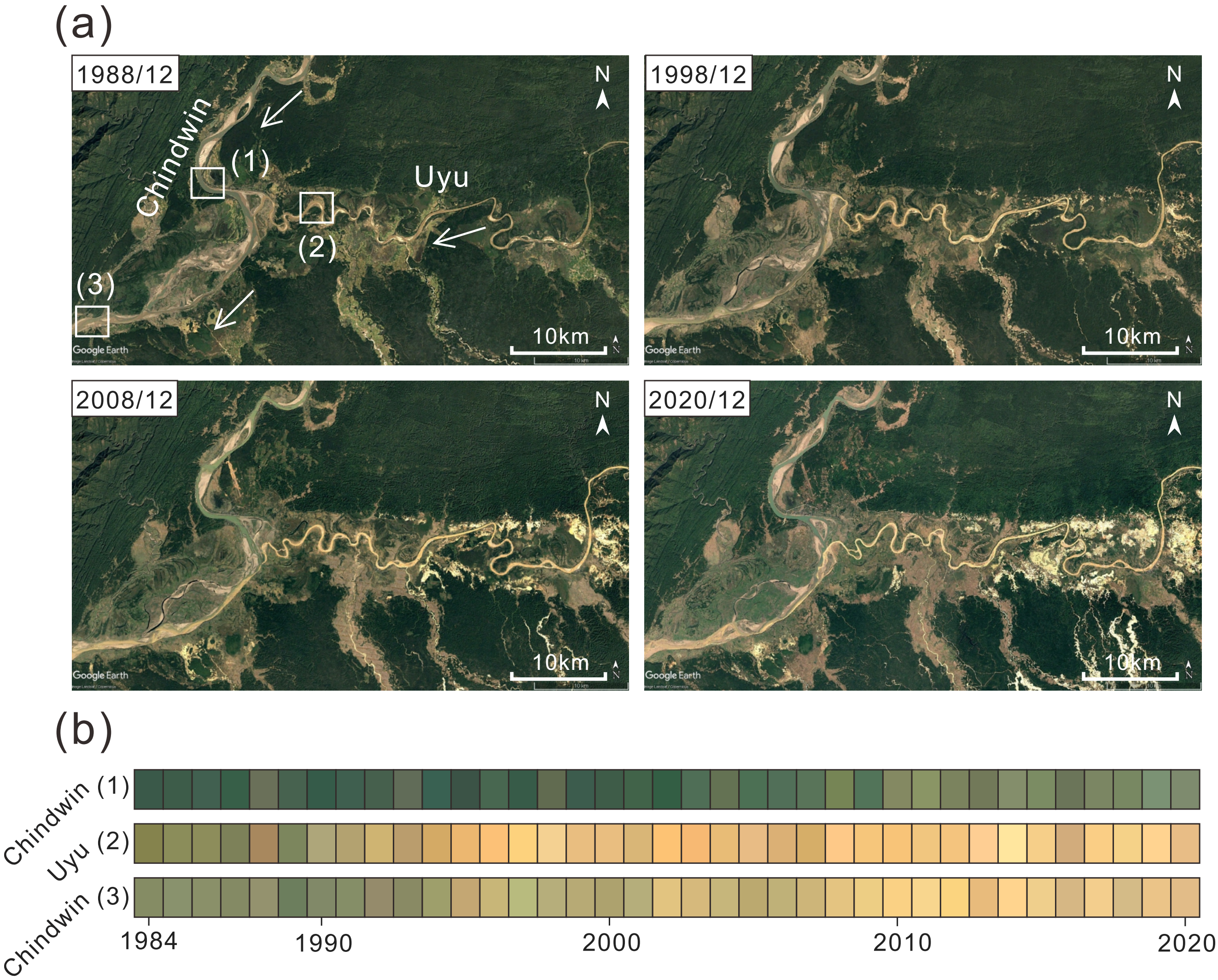

(a)
1988/12
Chindwin
(1)
(2)
(3)
Uyu
10km
1998/12
2008/12
2020/12
(b)
Chindwin (1)
Uyu (2)
Chindwin (3)
1984
1990
2000
2010
2020

Figure 9.

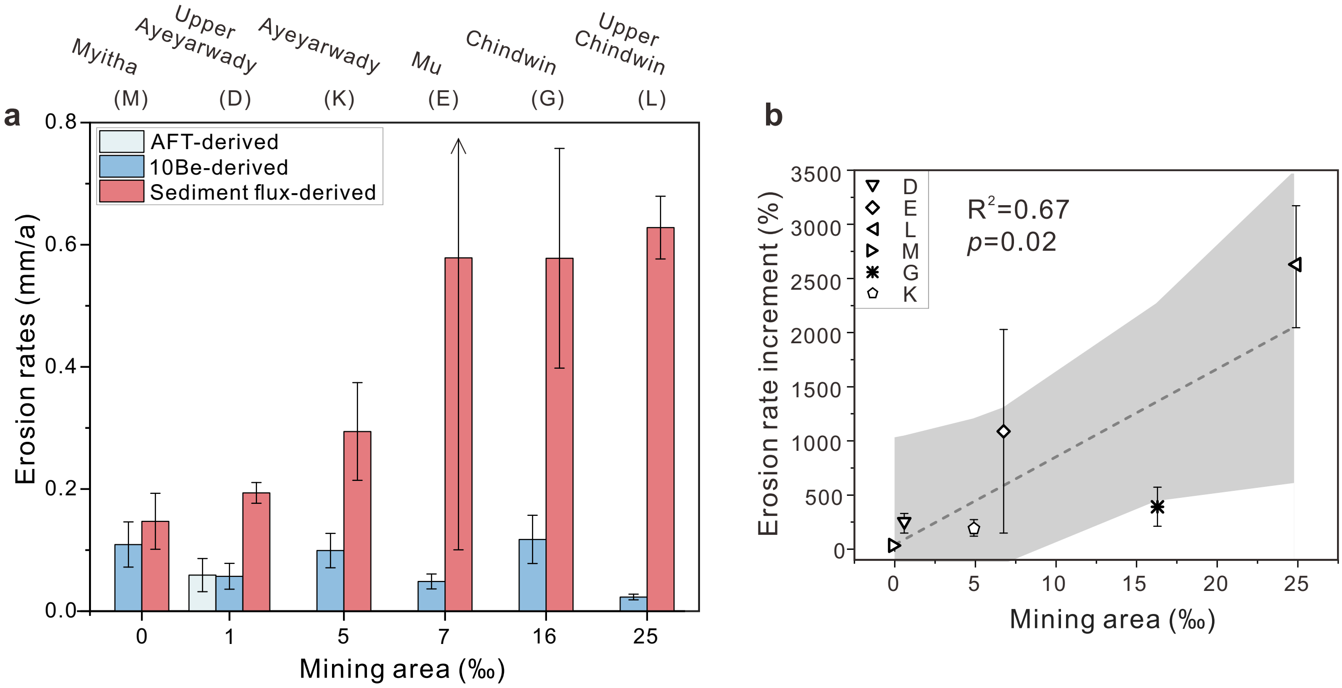

a
Myitha (M)
Upper Ayeyarwady (D)
Ayeyarwady (K)
Mu (E)
Chindwin (G)
Upper Chindwin (L)
AFT-derived
10Be-derived
Sediment flux-derived
Erosion rates (mm/a)
0.0
0.2
0.4
0.6
0.8
0
1
5
7
16
25
Mining area (‰)
b
D
E
L
M
G
K
R^2=0.67
p=0.02
Erosion rate increment (%)
0
500
1000
1500
2000
2500
3000
3500
0
5
10
15
20
25
Mining area (‰)

Table 1 Ayeyarwady catchments land use and land cover changes

Land type	Catchment	Previous area (km^2)	Recent area (km^2)	Changes (%)	Period	References
Forestry Coverage	Uyu			-8.90	1999-2019	McGinn et al. (2021)
	Upper Chindwin	636000	500000	-21.38	1988-2017	Yang et al. (2019)
	Lower Chindwin			4.60	1999-2019	McGinn et al. (2021)
	Chindwin	8804521	8576294	-2.59	1999-2019	McGinn et al. (2021)
	Upper Ayeyarwady	210700	162400	-22.92	1988-2017	Yang et al. (2019)
	Lower Ayeyarwady	54000	20100	-62.78	1988-2017	Yang et al. (2019)
	Total Myanmar	391705	381648	-2.57	1990-2020	Li et al. (2024)
Agriculture Coverage	Uyu			1.00	1999-2019	McGinn et al. (2021)
	Lower Chindwin			-10.40	1999-2019	McGinn et al. (2021)
	Chindwin	1229445	985161	-19.87	1999-2019	McGinn et al. (2021)
	Total Myanmar	152687	153117	0.28	1990-2020	Li et al. (2024)